Machine learning boiling prediction: From autonomous vision of flow visualization data to performance parameter theoretical modeling

Cho-Ning Huang [a], Sanghyeon Chang [b], Youngjoon Suh [b], Issam Mudawar [c], Yoonjin Won [b,d], Chirag R. Kharangate [a,*]

[a] *Department of Mechanical and Aerospace Engineering, Case Western Reserve University, 10900 Euclid Avenue, Cleveland, OH 44106, USA*
[b] *Department of Mechanical and Aerospace Engineering, University of California, Irvine, CA, USA*
[c] *School of Mechanical Engineering, Purdue University, West Lafayette, IN, USA*
[d] *Department of Electrical Engineering and Computer Science, University of California, Irvine, CA, USA*

ABSTRACT

Flow boiling is a highly efficient configuration for meeting the high heat dissipation demands of thermal management systems. However, the complex physics of two-phase flow has hindered its broader application, especially in terms of quantifying visual information. Recent advancements in machine learning vision tools have revolutionized the analysis of phase change phenomena by enabling the digitalization of physically meaningful features such as void fraction, vapor-liquid interfacial behaviors, and liquid-solid wall wetting front areas en masse. In this study, we systematically investigate two-phase models that compute void fractions, heat transfer coefficients, and critical heat flux using live bubble data streams under microgravity. The collected empirical bubble data is used to supplement and validate traditional control-volume-based theoretical modeling approaches. Void fraction data is first validated with analytical frameworks. This is followed by void fractions and wetting front areas being used to improve correlations predicting heat transfer coefficients. This work showcases the potential of using a new machine learning-based strategy to accelerate scientific formula discovery through the extraction of multi-level and physically meaningful features.

1. Introduction

Due to the significant advancement in high-performance electronic applications over the past few decades, it has become difficult for traditional single-phase thermal management systems to meet the new heat dissipation requirements. In comparison to single-phase systems, two-phase thermal management systems include phase change that involves latent heat exchange leading to a significant improvement in heat transfer capacity. There are many phase-change thermal management configurations developed by researchers. Heat pipes are the most widely-used thermal management configurations for various thermal applications (Sauciuc et al., 1996; Delil, 2003; Huang et al., 2023; 2021) due to their low costs, high efficiency, and simplicity. The use of mini/ microchannel, taking advantage of pumped flow, can further enhance the cooling performance (Okawa, 2012; Koşar et al., 2005; Escher et al., 2009; Ohadi et al., 2013) while other cooling schemes such as jet-impingement (Huang and El-Genk, 1994; Polat et al., 1989) and spray cooling (Horacek et al., 2005; Kim, 2007) are more aggressive and can provide even higher heat transfer coefficients.

Understanding and designing heat acquisition systems utilizing flow boiling is crucial to the widespread implementation of phase-change in these thermal management systems. Across phase-change configurations, the most common approach to predicting performance parameters such as void fraction, heat transfer coefficient, and critical heat flux is empirical and semi-empirical correlations (Schrage et al., 1988; Kawahara et al., 2002; Katto, 1981; Oh and Son, 2010; Li and Wu, 2010; Li et al., 2023). These are based on experiments performed by researchers over a range of testing conditions based on working fluids, geometries, and flow parameters. These tools can lose their reliability outside the testing range due to the complex nonlinear physics involved in phase-change systems. An improved approach has been the use of universal correlations that are developed by consolidating databases which includes numerous working fluids, extensive ranges of geometries, and various solid/ fluid properties. Another useful approach is conducting full computational fluid dynamics (CFD) simulations (Polat et al., 1989; Polat et al., 1989). However, with the advantage of high fidelity, CFD can be both cost and time ineffective. Theoretical and analytical models

---

Nomenclature

A	Cross-sectional area of flow channel (m^2)
Bo	Boiling number
Bd	Bond number
b	Ratio of wetting front length to wavelength in *Interfacial Lift-off Model*
$C_{f,i}$	Interfacial friction factor
$c_{p,f}$	Specific heat at constant pressure (J/kg-K)
D	Hydraulic diameter of flow channel (m)
Fr	Froude number
f_k	Friction factor for phase k
G	Mass velocity (kg/m^2-s)
g	Earth gravity (kg/m^2)
g_n	Normal component of Earth gravity(kg/m^2)
H	Height of flow channel's cross-section (m)
h	Heat transfer coefficient (W/m^2-K)
h_{fg}	Latent heat of vaporization (J/kg)
Ja	Jakob number
k	Thermal conductivity (W/m-K)
L_B	Length of the vapor blanket (m)
$\dot{m}$	Mass flow rate (kg/s)
MAE	Mean absolute error
p	Pressure (Pa)
P_{crit}	Critical pressure (Pa)
P_i	Interfacial perimeter (m)
P_F	Wetted perimeter (m)
P_H	Heated perimeter (m)
P_R	Reduced pressure (m)
Pr	Prandtl number
P_w	Wall friction perimeter (m)
q''_{CHF}	Critical heat flux (W/m^2)
q''_w	Wall heat flux (W/m^2)
Re	Reynolds number
S	Phase velocity ratio
T	Temperature (K)
$\Delta T_{sub,in}$	Inlet subcooling, T_{sat} - T_{in} (K)
U	Mean velocity (m/s)
u_i	Streamwise velocity of the liquid-vapor interface (m/s)
v	Specific volume (m^3/kg)
W	Width of flow channel and heated walls (m)
X_{tt}	Lockhart-Martinelli parameter
x	Quality
z	Axial coordinate (m)
z^*	Axial location for determining vapor layer critical wavelength (m)

Greek Symbols

α	Vapor void fraction
δ	Mean thickness of vapor layer (m)
λ	Wavelength (m)
λ_c	Interfacial instability critical wavelength (m)
ρ	Density (kg/m^3)
σ	Surface tension (N/m)
μ	Dynamic viscosity (Pa-s)
Γ_{fg}	Evaporation per unit distance
τ_i	Interfacial shear stress (Pa)
τ_w	Wall shear stress (Pa)

Subscripts

avg	Average
B	Vapor blanket
c	Critical; core
ex	Exit
exp	Experimental
f	Saturated liquid
g	Saturated vapor
h	Homogeneous model
i	Interfacial
k	Phase k, $k = f$ or g
ONB	Onset of nucleate boiling
$pred$	Predicted
sp	Single-phase
sub	Subcooling
tp	Two-phase
w	Heated wall

also provide good ways to predict the performance parameters by capturing the underlying physics behind the phenomenon with reduced computational costs. However, they must be verified by experiments to ensure their reliabilities for the conditions under investigation including flow regimes and thermal transport behaviors. Recently, soft computing techniques such as Artificial Neural Networking (ANN), Genetic Algorithm (GA), and various other statistical/ machine learning modalities (Nair et al., 2022; Anand et al., 2022; Qiu et al., 2021; Khosravi et al., 2018) have become popular and their results are showing promise in the validation and development of improved predicting tools for phase-change.

1.1. Flow boiling void fraction

For a flow boiling thermal management system, the flow consists of two phases, the liquid phase and the vapor/gas phase within the flow channel. An important parameter useful to system performance is the ratio between the area occupied by the vapor phase and the total area, called the vapor void fraction. At any axial location in the flow channel, the void fraction is defined as the cross-sectional area occupied by the vapor relative to the total cross-sectional area of the channel. The definition is shown in the following equation:

$$\alpha = \frac{A_g}{A_{total}}. \tag{1}$$

In most studies, the void fraction inside a flow channel is hard to measure directly, therefore, theoretical models and/or empirical correlations have been developed and used by researchers in the literature. Cai et al. (2021) did a comprehensive review for the void fraction models and correlations by classifying them into four different categories: *Modified Homogeneous Model, Slip Ratio Model, Drift-flux Model*, and *Empirical Correlations*. The simplest model that has been widely used is the *Homogeneous Equilibrium Model* (HEM). The void fraction is given by,

$$\alpha = \frac{1}{1 + \frac{\rho_g}{\rho_f}\left(\frac{1-x}{x}\right)S}. \tag{2}$$

where x is the quality and ρ is the density. In HEM, the velocities of the vapor phase and the liquid phase are assumed to be the same, leading to a velocity ratio, $S = u_g/u_f = 1$. This model is practical only when the velocity difference between phases is small or negligible, usually in the bubbly regions of the flow. Armand and Treščev (1959), Nishino and Yamazaki (西野晴生 and 山崎彌三郎, , 1963), and Chisholm (1983) developed a modified version of HEM to improve practicality. A popular

slip ratio model to predict the void fraction is proposed by Zivi (1964). This model is a kinetic energy model with the phase velocity ratio, S, equal to $(\rho_f / \rho_g)^{1/3}$ by utilizing the principle that in a steady state thermodynamic process the rate of entropy generation is minimum. Like the Zivi model, Fauske (1961) proposed that S is equal to $(\rho_f / \rho_g)^{1/2}$ to develop their model while Smith (1969) developed another model by equalizing the momentum fluxes of the two phases. Drift-flux models are relatively more attractive because they include radial velocity distribution, surface tension, and buoyancy effects in their formulations. The earliest drift-flux model was developed by Zuber and Findlay (1965). They accounted for the effect of the nonuniform flow as well as the effect of the local relative velocity between the phases to develop the model. Rohuani and Axelsson (1970) proposed their drift-flux model by describing the mechanism of the detaching bubbles from evaporation and calculating the rates of heat transfer for the vapor and liquid phases and the rate of vapor condensation in the liquid was also included in the development of the model. Kawahara et al. (2002) and Huq and Loth (1992) also provide empirical correlations that are simple to use. Both these correlations are empirical calibrations of the HEM. Beside these four categories, *Separated Flow Model* (SFM) is another approach to predicting void fraction by applying a control volume analysis to the flow channel (Zhang et al., 2007). In this model, the flow is divided into two layers, the vapor layer and the liquid layer, and the mass, momentum, and energy conservation equations are solved simultaneously. The velocity of each phase is assumed to be uniform in the axial (flow) direction, while allowing for a velocity difference between phases. Pressure is assumed to be uniform over the entire cross-section. These assumptions facilitate the analyses of individual phases. Based on this approach, SFM is intended mostly for annular and stratified horizontal flow regimes.

1.2. Flow boiling heat transfer coefficients

An important design parameter of interest in flow boiling is the heat transfer coefficient. This parameter is very difficult to predict because of its strong dependency on the flow regime. For example, heat transfer coefficient has slightly negative or no relationship to the vapor quality when the quality is low while this relationship becomes strongly negative at high vapor quality regimes (Collier and Thome, 1994). Moreover, the heat transfer coefficient will face a sudden reduction when critical heat flux or dryout occurs. Researchers have performed multiple experiments to develop heat transfer coefficient correlations specific to different flow boiling configurations. Lazarek and Black (1982) tested a round tube with R-113 as the working fluid and a correlation for the local heat transfer coefficient was developed based on their experimental data. Tran et al. (1996) tested both circular and rectangular channels with two kinds of refrigerants, R-12 and R-113 and heat transfer data for these two fluids were correlated and presented in the nucleation-dominant region. Gopinath et al. (2002) proposed two correlations in their study for both saturated and subcooled flow boiling based on their own experimental database. Similarly, Yu et al. (2002) and Ducoulombier et al. (2011) also provide their own correlation by performing their experiments. Other studies (Shah, 1982; Agostini and Bontemps, 2005; Cooper, 1984; Hamdar et al., 2010; Kenning and Cooper, 1989; Liu and Winterton, 1991; Li and Wu, 2010; Kim and Mudawar, 2013; Lazarek and Black, 1982; Tran et al., 1996; Yu et al., 2002; Kew and Cornwell, 1997) proposed their correlations by consolidating large databases generated by other researchers. In recent years, correlations and predicting tools developed using machine learning models have also been promising (Sun and Mishima, 2009; Naphon et al., 2018; Mehrabi et al., 2013; Ghahdarijani et al., 2017). Correlations are still the most common tools used for heat transfer coefficient predictions, but improvements are necessary for them to be able to be generalizable to a wide range of conditions.

1.3. Critical heat flux

In heat flux-controlled flow boiling systems and devices, critical heat flux (CHF) is another crucial design parameter. CHF, also known as the boiling crisis, is characterized by a sudden increase in the surface temperature and a significant reduction in heat transfer coefficient during flow boiling. CHF happens when the vapor generation on the heated surface is too high to allow bulk liquid access to the surface. This phenomenon can cause local burnout leading to catastrophic failure of the thermal management system. Like heat transfer coefficients, a common approach used in predicting CHF is the use of empirical correlations. By performing experiments with specific working fluids and under certain operating conditions, CHF correlations can be developed and become reliable enough to make design decisions. One of the earliest works was done by Katto (1981). In his study, the working fluids were water, Freon-21. Freon-12, Freon-114, liquid nitrogen, liquid helium, and liquid parahydrogen. By consolidating several vertical upflow experimental data points, Katto developed a general correlation of CHF for zero inlet subcooled flow which provided an accuracy R of $0.969 < R < 1.47$. Later, Katto (Katto and Ohno, 1984) continued his work on the correlations by adding more data points and improved the accuracy to R of $0.945 < R < 1.071$. Lazarek and Black (1982) performed a series of experiments with a round tube of both vertical upflow and vertical downflow configurations, and proposed a correlation based on their data that produced an accuracy within ± 10 %. Oh and Englert (1993) developed a correlation for rectangular flow channel with standard deviation of 17 % and 19 % for upflow and downflow experiments, respectively. Some other well-known correlations by Bowring (1972), Tan et al. (2017), and Tong (1968) have also been widely used over the past few decades. A major drawback of empirical correlations are their limitations to predict only within the parameter ranges they were developed for. A better approach for predicting CHF is the use of the theoretical or mechanistic models shown in Fig. 1. Theoretical models are developed by capturing the flow physics and depend on a trigger mechanism for estimating the CHF value. Kutateladze and Leont'ev (1966) postulated one of the oldest theoretical CHF models, the *Boundary Layer Separation Model*, for estimating flow boiling CHF. The trigger mechanism for CHF was the forward liquid motion obstructed by the heated wall vapor production. Weisman and Pei (1983) proposed the *Bubble Crowding Model*. According to the model, CHF occurs when the bubbles start crowding the bubbly layer hampering liquid from moving to the heated wall. The *Sublayer Dryout Model* was postulated by Lee and Mudawwar (1988). The authors claimed that the bubbles coalesce into oblong vapor patches under the liquid sublayer close to the wall triggering CHF, and CHF point occurs when the input energy exceeds the enthalpy of the liquid from the sublayer. Galloway and Mudawar (1993) postulated the *Interfacial Lift-off Model* by calculating the net momentum of the wavy interface between the vapor and the liquid. By assuming the ratio between the wetting front (liquid to heated wall contact area) and the wavelength to be equal to 20 %, the CHF was estimated. This model has been validated by various researchers but has limitations at low mass flow rates (Zhang et al., 2005; Kharangate et al., 2016; Konishi et al., 2015). Liu and Nariai (2000) developed a model based on the observations of the vapor blanket and the liquid sublayer close to the heated wall. The wavelength of the vapor blanket is assumed to be equal to the Helmholtz instability wavelengths at the liquid-gas interface. According to the model, CHF occurs when the liquid sublayer is vaporized by the surface energy. Most recently, Huang and Kharangate (2019), (2020) proposed the *Hydrodynamic Instability-based CHF Model*. The model describes a wavy vapor layer that prevents liquid from contacting the heat dissipated wall. Combining Taylor's stability of interface as well as Helmholtz instability of Zuber pool boiling, the model predicts CHF and showed very good agreement compared to experimental data.
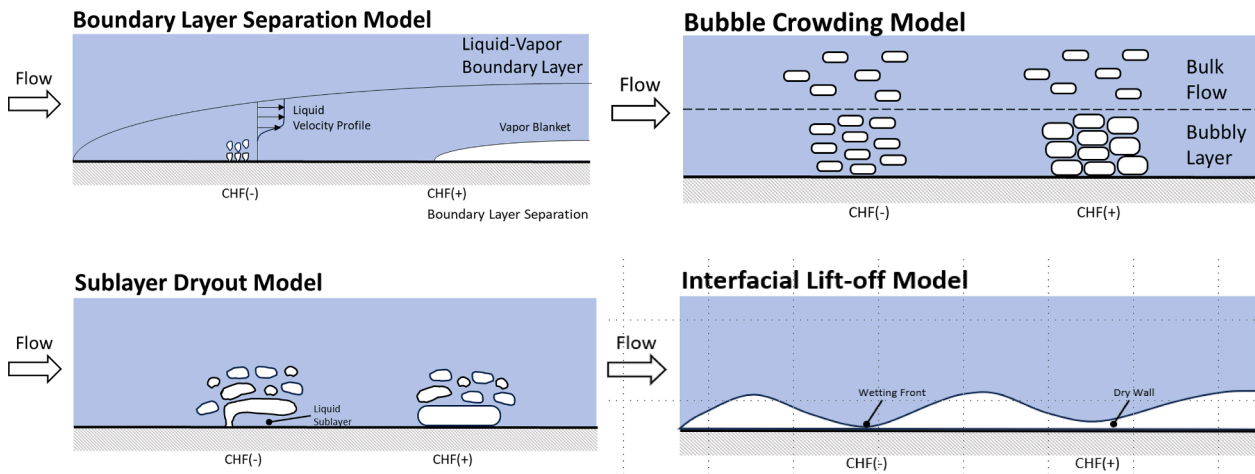
Fig. 1. Flow boiling critical heat flux mechanistic theoretical models from literature (Weisman and Pei, 1983; Lee and Mudawwar, 1988; Galloway and Mudawar, 1993; Zhang et al., 2005).

1.4. Machine learning methods

While the previous work has focused on the empirical correlations, which necessitate numerous data points for thorough analysis, there exists a gap in identifying the pertinent physical features. Traditional data and acquisition methods have proven inadequate in accurately capturing these features essential for modeling flow. This might be soon addressed by averaging modern data analysis or machine learning (ML) strategies. In the past three decades, we have seen unprecedented development of soft computing techniques, such as Genetic Programming (GP), Fuzzy-logic Control, and Data Mining that can be applied to many scientific and engineering practices. However, their application to the inference of two-phase experiments data, particularly flow boiling, has been limited. A multitude of two-phase experiments in the past have utilized high-speed flow visualization as an important diagnostic tool to capture temporal and spatial two-phase interfacial features during phase-change, yet the majority of these features have traditionally been determined through manual analysis or rudimentary algorithmic approaches which requires significant human involvement. By integrating ML-based framework, we demonstrate in this work that we can automate this process, allowing for the analysis of significantly larger datasets. Therefore, we capture new data on void fraction, bubbles, interfacial behaviors, and wetting fronts in flow boiling based on data from high-speed cameras (Chang et al., 2023). Ten different features were computed based on 30,000 flow boiling images under microgravity. This data can help us validate and model flow boiling performance parameters with reasonable accuracy.

1.5. Objective of study

Flow boiling performance parameter predictions are important but modeling tools currently available have limitations in their prediction capabilities and generalizability. In a recent study, our team developed a novel ML-enabled tool to autonomously capture two-phase behaviors from flow boiling imaging data (Chang et al., 2023). This study is a follow-up investigation on utilizing and predicting performance parameters of interest to flow boiling using this new data. The statistically averaged information relating to void fraction, bubble behaviors, interfacial waviness, and wetting fronts will be analyzed and correlated with performance parameters including void fraction, heat transfer coefficient, and critical heat flux. The data are used in combination with traditional modeling techniques to demonstrate the development of improved prediction tools, theoretical models and correlations. This study will also lay the groundwork for future validations of widely available traditional flow boiling imaging data from multiple studies in the literature for developing universal models for identifying phase-change performance parameters.

2. Experimental module

The visual and numerical data analyzed and modeled in this study is obtained from Purdue University Boiling and Two-Phase Flow Laboratory's (PU-BTPFL's) experimental database. The specific data used here is based on Konishi et al. (2015) with FC-72 as the working fluid in a rectangular single-sided heating flow boiling configuration with mass flow rates of 10, 20, and 40 g/s under microgravity conditions in a parabolic flight. Fig. 2(a) adapted shows the schematic of the flow-conditioning loop that provides the specific inlet temperature and pressure conditions for the fluid entering the flow boiling module. The flow boiling module is the main component of the flow conditioning loop and is used to obtain data for wall temperature, pressure drops, CHF, and interfacial behaviors. Type-E thermocouples with an accuracy of ± 0.5 °C are used to measure the fluid and wall temperature throughout the flow boiling loop. Pressure at several locations along the FBM and the flow loop are measured by STS absolute pressure transducers with an accuracy of ± 0.05 %. Fig. 2(b)-(c) shows the details of the flow boiling module that allows both single-sided and double-side heating capability. The flow channel has a rectangular cross-section with a width equal to 2.5 mm and a height equal to 5.0 mm. Resistive heaters are attached to copper blocks on both the top and bottom sides of the flow channel to ensure uniform heat flux. Thermocouples are connected to the heated section to measure the wall temperature. Absolute pressure transducers were used to measure the pressure drop across the heated flow channel. Fig. 2(d)-(f) shows pictures of the three flow boiling facilities whose experimental data is being utilized in this study. A complete description of the flow-conditioning loop and the flow boiling modules can be found in the following articles (Konishi et al., 2015; Zhang et al., 2002; Kharangate et al., 2015).

## 3. Machine learning-assisted analysis

The ML-enabled framework consists of object detection, object tracking, and data processing modules to autonomously detect and record the spatiotemporal statistics of bubbles during flow boiling as shown in Fig. 3(a). First, high-resolution flow boiling images are passed through a custom-trained Mask R-CNN model where instance-specific bubble masks are generated in the object detection and segmentation module (Suh et al., 2021). The Mask R-CNN model in this study is trained over 100 epochs using stochastic gradient descent, with a learning rate of 0.0008 and a momentum of 0.9. To comprehend the
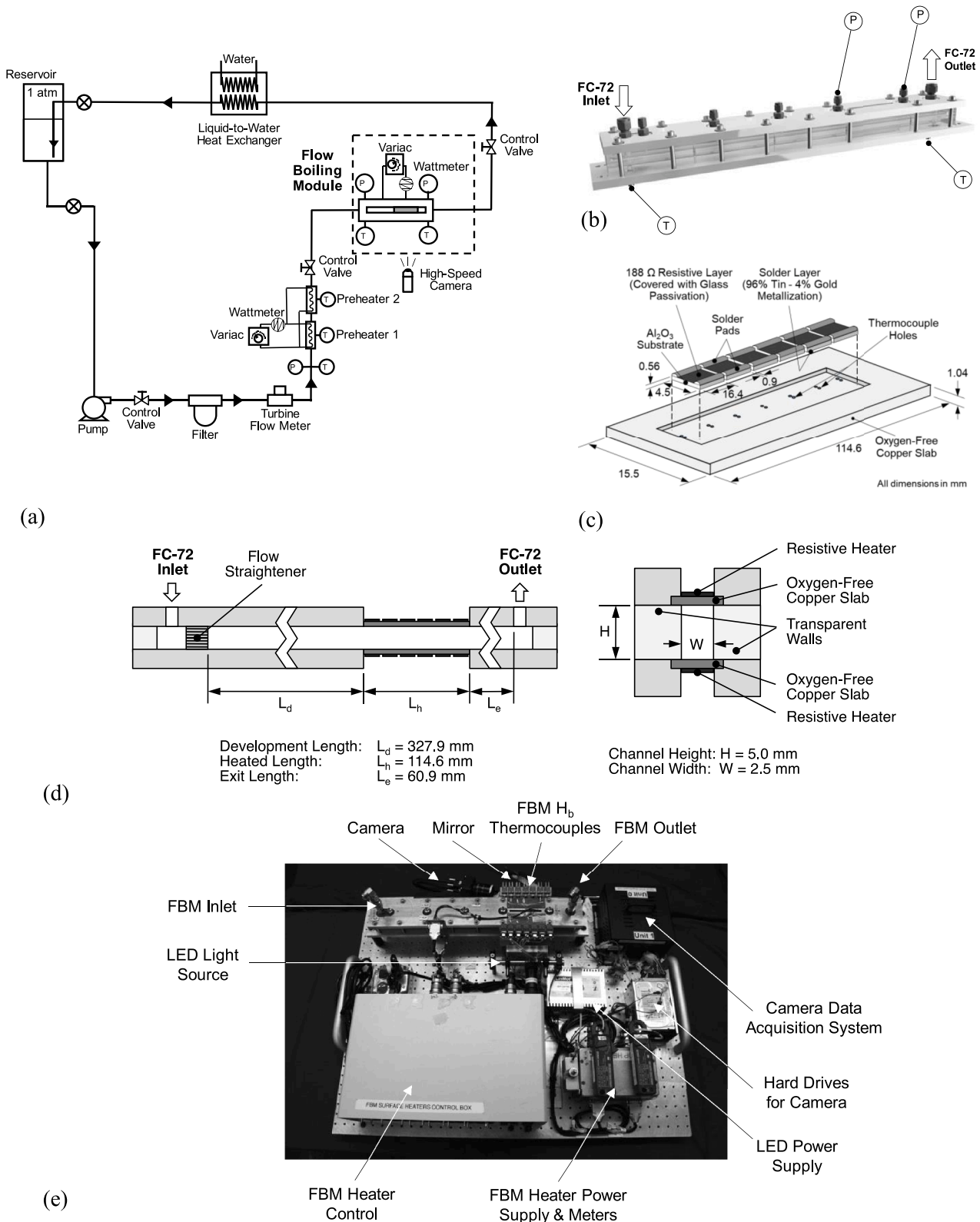
Fig. 2. (a) Schematic of the flow loop. (b) Assembled view of the flow boiling module. (c) Heater wall construction. (d) Key dimensions of the flow channel. (e) Photo of the flow boiling loop. Adapted from Kharangate et al. (Suh et al., 2021).

model's predictions, its performance is assessed through the examination of typical evaluation metrics like recall, precision, accuracy, and F1 Score. The model showcases outstanding detection abilities, achieving scores above 87 % for these standard metrics and providing a reliably precise measurement through the MAPA metric, with a score exceeding 94 % (Chang et al., 2023). Subsequently, the object tracking module processes these detected masks, linking unique identifiers (IDs) over time. The tracked information is then post-processed through a data
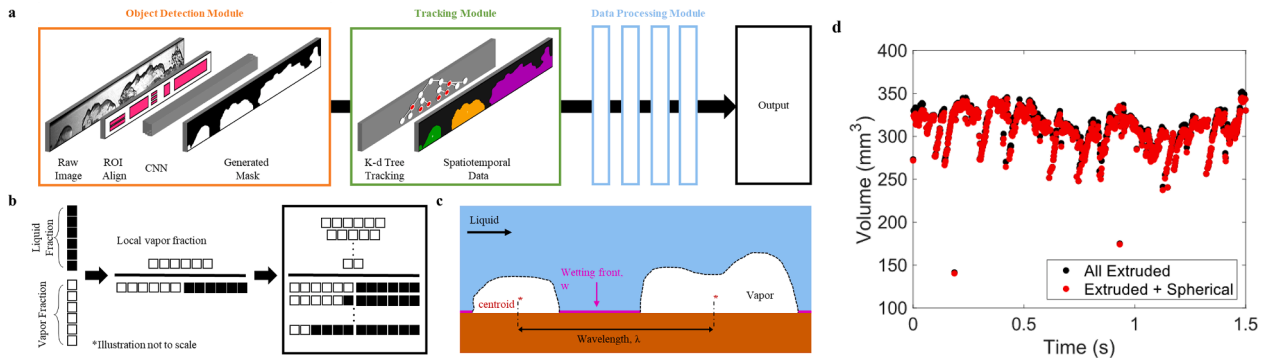
Fig. 3. Vision-based deep learning framework: (a) The framework consists of object detection, tracking and data processing modules to automatically detect bubbles and extract physically meaningful quantities. (b) In the data processing module, vapor fraction is obtained by tabulating white pixels (representing vapor) and black pixels (representing working fluid). The data processing module computes the features, such as wavelength and wetting front, as illustrated in (c). Schematics are not to scale. (d) Comparison of volume fraction estimations for 10 g/s case with 70 % of CHF between two scenarios: All vapor is assumed 2D and extruded in the 3D plane to extract the void fraction (black), and small bubbles are assumed to be hemispherical shape while larger bubbles > 2.5 mm are extruded in the 3D plane (red). The results indicated a 0.8 % difference in estimated volume

processing module where the meaningful and spatiotemporal features are gathered through in-house algorithms (Suh et al., 2021).

To elaborate, the vapor fraction is calculated by dividing the vapor area by the total area of the channel as shown in Fig. 3(b). Binarization techniques are employed to differentiate the vapor and liquid regimes. The wetting front is quantified by measuring the distance between bubbles at the liquid-solid interfaces. The wavelength is computed by calculating the distance between the centroids of two adjacent bubbles illustrated in Fig. 3(c). Upon the completion of pixel quantification, the length measurements in terms of pixels are converted into millimeter-scale dimensions. Detailed information regarding the framework can be found elsewhere (Suh et al., 2023).

Physical features such as void fraction, wetting front, and wavelength are extracted by analyzing binarized images obtained from the object detection module. At this stage, the vapor and liquid phases in these images can be clearly distinguished by the segmentation model and can be post-processed using relatively simple algorithms. Because vapor (bubble) and liquid (working fluid) regions are represented by white and black pixels, respectively, the vapor fraction can be calculated by tabulating the ratio between the white pixels (vapor) and total pixels as shown in Fig. 3(b):

$$\text{Local void fraction} = \frac{\text{White pixels in column at location } x}{\text{Total number of pixel in column at location } x} \tag{3}$$

The wetting front is quantified by counting the number of black pixels at liquid-solid interfaces. The wavelength is computed by calculating the distance between the centroids of two adjacent bubbles illustrated in Fig. 3(c). Upon the completion of pixel quantification, the length measurements in terms of pixels are converted into millimeter-scale dimensions (Chang et al., 2023). Based on the study by Ren et al. (2015), objects can be entirely segmented from the background with pixel-level accuracy. The accuracy for single object detection is proved to be more than 97 % by applying the EfficientDet algorithm with three BiFPN layers is used for hierarchical feature extraction and three convolutional layers are used for the shared box prediction section. We make a 2D assumption for the analysis which seems to be valid for larger vapor voids but might lead to errors when we have smaller bubbles like in the wetting fronts. Since a channel depth of 2.5 mm is significantly smaller than a channel length of 80 mm, our analysis shows that the vapor fraction can be calculated reasonably well based on the two-dimensional assumption. To assess the validity of two-dimensional assumption, we compared the cumulative volume of bubbles within the channel in two scenarios. One, when all bubbles are assumed to have fully extruded shapes by applying *Volume = Area*Depth* (which is fully

2D assumption), where depth refers to the channel depth which is 2.5 mm. Two, when we assume a hemispherical shape for bubble diameters smaller than the depth of the channel, assuming no contact with the surrounding wall by using *Volume* $= \pi D_{eq}^3/6$ where D_{eq} is the equivalent closest spherical diameter for the small bubbles. In this second scenario, we still use fully 2D assumption for the larger bubbles. When we compare the two results, we only observe a 0.8 % difference in average void fraction estimation, as shown in Fig. 3(d). This difference is statistically insignificant in terms of the vapor proportion. Therefore, we can assume that the assumption of floating bubbles for small sizes is a reasonable way to get an accurate estimation of the void fraction in this scenario.

4. Results and discussion

The main purpose of this study is to apply the experimental data captured by machine learning algorithms (Chang et al., 2023) into models and correlations for estimating void fraction, heat transfer coefficient, and CHF during flow boiling.

4.1. Void fraction

First, we investigate the void fraction. The statistical spread and average void fraction captured using the vision tool for three of the test cases are shown in Fig. 3. Fig. 4(a) illustrates the case for a mass flow rate of around 20 g/s and surface heat flux equal to 23.02 W/cm², which is 77 % of CHF, for flow boiling image data obtained from the experiments performed by Konishi et al. (2015). As shown in the flow images, the void fraction fluctuates between images as the vapor void fraction behavior is wavy with discontinuous vapor patches moving along the channel moving along with the liquid. Therefore, despite the increase in vapor generation moving downstream in the flow channel, various regions of the heated surface remain in direct contact with the liquid. These parts are called wetting fronts. The line shown in Fig. 4(a) is the void fraction averaged over 3,000 images captured at 2,000 frames per second, and the gray band depicts its standard deviation. Similarly in Fig. 4(b) and (c), as we go to higher velocities, we can see that the rate of void fraction growth and spread reduces with flow rate. The reduction in growth rate and the reduction in standard deviation is due to higher shear stress at higher flow velocities. The same procedure was used to capture void fractions for all the tests conducted in this investigation.

The captured experimental data can be validated with the models and empirical correlations described in Section 1.1 where we introduce prior void fraction models from literature. MAE to compare the experimental data obtained from the vision tool with the models is defined as
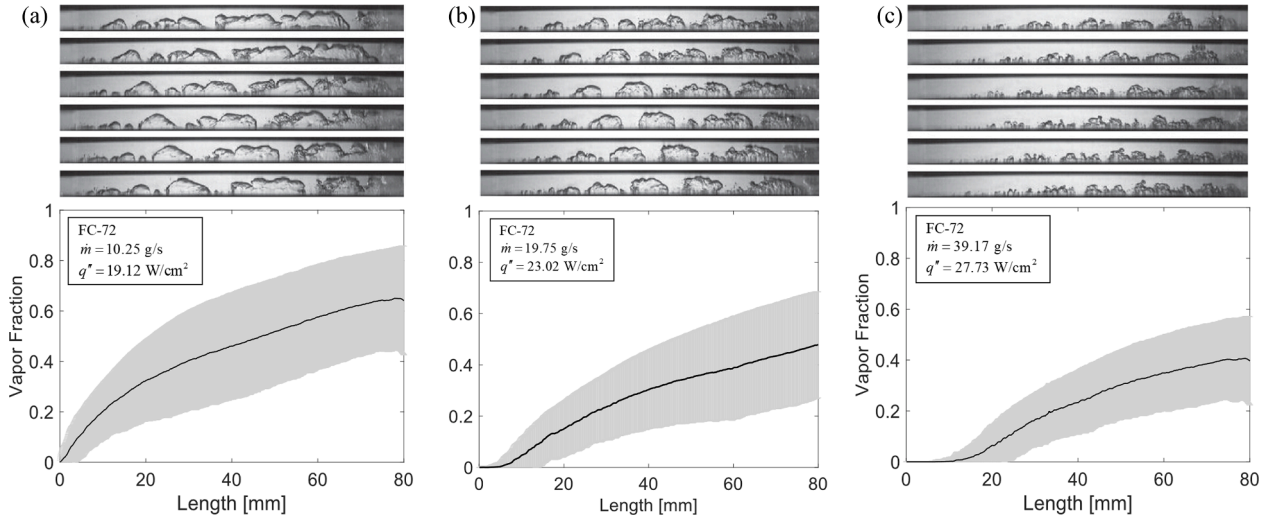
Fig. 4. Captured experimental data based on the vision tool with error for (a) mass flow rate 10.25 g/s with 76 % of CHF, (b) mass flow rate 19.75 g/s with 77 % of CHF, and (c) mass flow rate 39.17 with 77 % of CHF.

follows:

$$MAE = \frac{1}{N} \sum_{i=1}^{N} \frac{\left| \alpha_{i,\text{exp}} - \alpha_{i,\text{model}} \right|}{\alpha_{i,\text{exp}}}. \tag{4}$$

The specific equations for all the models and correlations are listed in Table 1. Fig. 5 illustrates the void fraction predictions using the best performing models and correlations with the experimental data for one of the test cases where the mass flow rate of 10 g/s and surface heat flux equal to 19.1 W/cm², which is 70 % of critical heat flux. The best predicting models within each group include modified homogeneous models, slip ratio models, drift-flux models, and correlations as well as the individual HEM and SFM models. The experimental α data below 0.05 (5 % of the channel height) was excluded from data validation/ error comparison because the vapor thickness as well as bubbles are too small to be captured accurately before the formation of a clear vapor blanket in the channel. In addition, the low void fraction data can be inaccurate because it is observed that the region close to the heated surface is slightly blurred from the original image data obtained by Konishi et al. (2015) in their experiments. It should also be noted that all models and correlations predictions shown in Fig. 5 have been adjusted with the overlap point for void fraction being the *z* location where void fraction is 5 % of the channel height. To clarify, we not only start at the 5 % void fraction for validation, but we also adjust the longitudinal location of this starting point to match the experimental data. This is deemed necessary because none of these models can capture the onset of nucleate boiling point accurately and no prior correlations were developed for this working fluid in this specific configuration. As a result, the data obtained from Fig. 4 is adjusted in the longitudinal direction to cross the 5 % reference void fraction point and then used for validation across the channel. As shown in Fig. 5, all the predicted curves cross with each other at the same location as the first data point. *Separated Flow Model* shows the best performance with the lowest MAE equal to 3.23 %. The SFM is the only model that accounts for the actual flow configuration with a control volume analysis predicting the phase velocities and void fraction along the channel. This is followed by the model by Nishino and Yamazaki (西野晴生 and 山崎彌三郎, 1963) with MAE equal to 6.26 %. Their model successfully modifies the HEMby including a slip ratio correlated with their experimental data. Rohuani and Axelsson (1970)'s model also shows good agreement evidenced by an MAE equal to 7.58 % as it accounts for the correct velocity distributions in both phases. Smith (1969) and Huq and Loth (1992) provide close MAEs of 10.77 % and 15.37 %, respectively. The HEM does not perform so well as shown in Fig. 4 with MAE equal to 53.09 %. The reason for its

poor performance is the unsuitable assumption that the phase velocities are equal which is typically only valid in the bubbly and the dispersed droplet flow regimes. The observed flow for our case is more in the wavy-separated regime. The averaged MAEs computed based on all the 10 experimental test cases are listed in Table 1. Validated by the experimental data, the *Separated Flow Model* provides the lowest overall MAE which is equal to 3.8 % while the *Homogeneous Equilibrium Model* has the poorest MAE of 59.3 %.

Fig. 6 compares the predictions for all the individual test cases for which we obtained data from the vision tool based on the *Separated Flow Model*. High-speed video images adapted from Konishi et al. (2015) are also included in Fig. 6 for reference. The *Separated Flow Model* performs remarkably well not only in capturing the overall MAE but also the local behavior along the channel with flow rate and heat flux. For the lowest flow rate, the model initially slightly underpredicts but its predictions improve as we move along the channel towards the exit. The higher flow rates have much better predictions along the full channel with good agreements between experimental data and the model predictions. However, it should again be noted that the onset of nucleation point was not captured by the modeling tool. When we do not adjust the longitudinal location to the 5 % void fraction data point, the *Separated Flow Model* is only able to capture the trend along the channel but not the exact local behavior. We investigated various correlations for onset of nucleate boiling but were unsuccessful. The main reason is that there is no prior correlation specific to this configuration or the working field in the literature. In conclusion, the experimental data of void fraction obtained from machine learning algorithms are helpful to validate the models and correlations with the *Separated Flow Model* providing the best predictions among the tested models and correlations.

In terms of limitations of this assessment, we should note that our ML framework and the validated models are developed for flow conditions that have a dominant separated liquid-vapor domain. Utilizing this for similar testing conditions would not require any retraining. While this framework is valid for the regimes with the existence of distinct liquid-vapor interfaces such as stratified and annular regimes, it will have limited applicability to other flow regimes like churn flow regime. The void fraction models and correlations need to be reassessed to check applicability. Therefore, more experimental imaging data across more geometric and testing conditions can help make this model more generalizable.

Table 1
Models and correlations for predicting void fraction.

Models/ Correlations	Equation	MAE
Homogeneous Model		
Homogeneous Equilibrium	$\alpha_H = \dfrac{1}{1 + \dfrac{\rho_g}{\rho_f}\left(\dfrac{1-x}{x}\right)}$	59.3 %
Modified Homogeneous Model		
(Armand and Treščev, 1959)	$\alpha = (0.833 + 0.164x)\alpha_H$	35.1 %
Nishino & Yamazaki (西野 晴生 and 山崎彌三郎, 1963)	$\alpha = 1 - \left(\dfrac{1-x}{x}\dfrac{\rho_g}{\rho_f}\alpha_H\right)^{0.5}$	6.8 %
(Chisholm, 1983)	$\alpha = \dfrac{\alpha_H}{\alpha_H + (1-\alpha_H)^{0.5}}$	32.5 %
Slip Ratio Model		
(Fauske, 1961)	$\alpha = \dfrac{1}{1 + \left(\dfrac{1-x}{x}\right)\left(\dfrac{\rho_g}{\rho_f}\right)^{0.5}}$	47.6 %
(Zivi, 1964)	$\alpha = \dfrac{1}{1 + \left(\dfrac{1-x}{x}\right)\left(\dfrac{\rho_g}{\rho_f}\right)^{2/3}}$	18.5 %
(Smith, 1969)	$\alpha = \dfrac{1}{1 + 0.79\left(\dfrac{1-x}{x}\right)^{0.78}\left(\dfrac{\rho_g}{\rho_f}\right)^{0.58}}$	13.5 %
Drift-flux Model		
(Rohuani and Axelsson, 1970)	$\alpha = \dfrac{x}{\rho_g}\{[1 + 0.12(1-x)]\left(\dfrac{x}{\rho_g} + \dfrac{1-x}{\rho_f}\right) + \dfrac{1.18(1-x)\left[g\sigma(\rho_f - \rho_g)^{0.25}\right]}{G\rho_f^{0.5}}\}^{-1}$	20.7 %
(Zuber and Findlay, 1965)	$\alpha = \dfrac{x}{1.2\left[x + \dfrac{\rho_g}{\rho_f}(1-x)\right] + \dfrac{0.35\rho_g\sqrt{gD}}{G}}$	32.1 %
Empirical Correlation		
(Huq and Loth, 1992)	$\alpha = 1 - \dfrac{2(1-x)^2}{1 - 2x + \left[1 + 4x(1-x)(\rho_f/\rho_g - 1)\right]^{0.5}}$	20.25 %
(Kawahara et al., 2002)	$\alpha = \dfrac{0.03\left[1 + \left(\dfrac{1-x}{x}\right)\dfrac{\rho_g}{\rho_f}\right]^{-0.5}}{1 - 0.97\left[1 + \left(\dfrac{1-x}{x}\right)\dfrac{\rho_g}{\rho_f}\right]^{-0.5}}$	52.4 %
Separated Flow Model (Zhang et al., 2007)		3.8 %

Momentum conservation:

$$G^2\frac{d}{dz}\left[\frac{(1-x_a)^2}{\rho_f(1-\alpha_a)}\right] = -(1-\alpha_a)\frac{dp}{dz} - \frac{\tau_{w,f}P_{w,f}}{A} \pm \frac{\tau_{ia}P_{ia}}{A} - \rho_f(1-\alpha_a)g\sin\theta$$

$$G^2\frac{d}{dz}\left[\frac{x_a^2}{\rho_g\alpha_a}\right] = -\alpha_a\frac{dp}{dz} - \frac{\tau_{w,g}P_{w,g}}{A} \mp \frac{\tau_{ia}P_{ia}}{A} - \rho_g\alpha_a g\sin\theta$$

Energy conservation: $\dfrac{dx_a}{dz} = \dfrac{q_w''W}{\dot{m}\left(c_{pf}\Delta T_{sub,in} + h_{fg}\right)}$

Wall shear stress equations: $\tau_{w,k} = \dfrac{1}{2}\rho_k U_k^2 f_k$

where the friction factor f_k is given by $f_k = C_1 + \dfrac{C_2}{Re_{D_k}^{1/C_3}} = C_1 + \dfrac{C_2}{\left(\dfrac{\rho_k U_k D_k}{\mu_k}\right)^{1/C_3}}$

where $k = f$ or g. $C_1 = 0$, $C_2 = 16$ and $C_3 = 1$ for laminar flow ($Re_{D_k} \leq 2100$), $C_1 = 0.0054$, $C_2 = 2.3 \times 10^{-8}$ and $C_3 = -2/3$ for transitional flow ($2100 < Re_{D_k} \leq 4000$), and $C_1 = 0.00128$, $C_2 = 0.1143$ and $C_3 = 3.2154$ for turbulent flow ($Re_{D_k} > 4000$) and where $D_k = 4A_k/P_k$

Interfacial shear stress equations: $\tau_{ia} = \dfrac{C_{f,ia}}{2}\rho_g(U_{ga} - U_f)^2$ and $\tau_{ib} = \dfrac{C_{f,ib}}{2}\rho_g(U_{gb} - U_f)^2$

where $C_{f,ia} = C_{f,ib} = 0.5$

4.2. Heat transfer coefficients

This section examines the accuracy of heat transfer coefficient by comparing different correlations with experimental data, highlighting the variations and consistencies in the analysis of thermal system performance. Several commonly used correlations for flow boiling are listed in Table 2. Fig. 7(a) illustrates all the predictions based on the correlations in Table 2 and the comparison with experimental data for the test
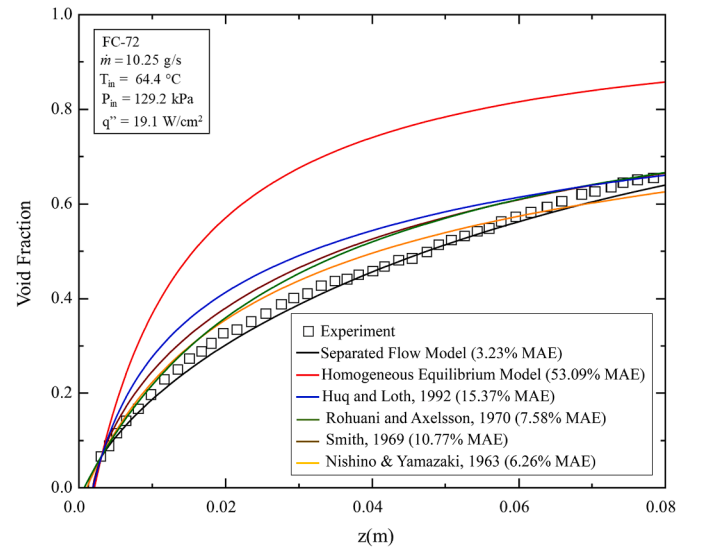

Fig. 5. Void fraction comparisons between experimental data and predictions based on various models and correlations.

case with a mass flow rate of 10 g/s and surface heat flux equal to 19.1 W/cm². It can be observed that some of the correlations such as the one by Hamdar et al. (2010) provide a reasonable prediction in terms of the averaged heat transfer. This can be attributed to their study using a similar working fluid and channel geometry. Some other correlation predictions such as Li and Wu (2010), Kim and Mudawar (2013) and Liu and Winterton (1991) while not matching the performance of Hamdar et al., also perform well on the averaged predictions as they pertain information on the working fluid in their theory. Correlations such as Lazarek and Black (1982) and Tran et al. (1996) do not do so well. The significant differences between the correlations and experiments can be attributed to the tested geometry configuration of the flow channel in their experiments. Both these studies used circular tubes and not the rectangular channels with non-uniform heating. However, as we can clearly see that although the averaged heat transfer coefficient is reasonable for many correlations, none of them capture the trend which is a reduction in heat transfer coefficient along the channel as observed in the experimental data. Specifically, as observed in the images in Fig. 6, the vapor thickness is increasing, and the liquid wetting front lengths are reducing as we move downstream along the channel. This behavior should impact the thermal transport capability along the channel, something the prior correlations are not able to account for. It was observed that while all experimental data was seen to reduce in the flow direction all correlations predicted either an increase or more or less constant variation in the downstream direction. Similar behaviors are observed in Fig. 7 (b) which illustrates the case with mass flow rate equal to 19.76 g/s and heat flux equal to 23.17 W/cm² (77 % of CHF).

Therefore, we can see that the correlation models are not able to account for how the liquid and vapor phases behave in the flow channel. We can try to capture the actual behavior we observe using the schematic of the flow in Fig. 8. The flow channel consists of continuous regions of vapor patches and wetting fronts moving along the flow channel with the liquid, with two such segments depicted in the figure. What we observe is that at any point in time, the wall is either exposed to the wetting front or to a complete vapor patch. Using the ML vision tool, we can capture the lengths of the wetting fronts and the corresponding vapor patch lengths. The wetting front's information along the channel for all the test cases is shown in Fig. 9(a), (b), and (c) corresponding to mass flow rates around 10 g/s, 20 g/s, and 40 g/s, respectively. Like the data on void fraction this number is averaged over 30,000 images by the ML vision tool. The whole flow channel is subdivided into 10 sections equally, so the length of each section is equal to 8 mm. In Fig. 9(a), we

(a)   (b)   (c)
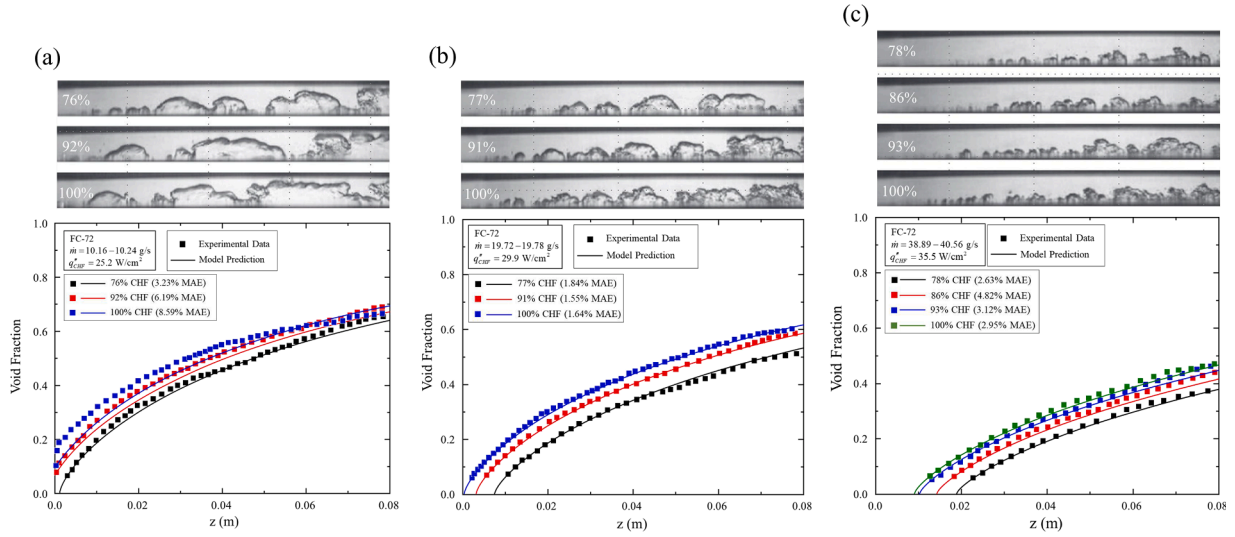
Fig. 6. Comparison between Separated Flow Model predictions and the experimental data for (a) mass flow rate around 10 g/s, (b) mass flow rate around 20 g/s, and (c) mass flow rate around 40 g/s.

see that for the case of 10 g/s wetting front length decreases as we move downstream. This is caused by the increase in vapor accumulation as we add more heat to the boiling fluid. Exit sections of the channels show wetting fronts rations of under 10 %. In addition, as we increase the heat flux, the wetting front reduces at each location along the channel with CHF critical heat flux showing the smallest wetting front lengths. This is also expected as we add more heat, we increase the vapor accumulation on the heated wall. Similar behaviors can be seen in Fig. 9(b) and (c) showing wetting front length ratios corresponding to 20 g/s and 40 g/s, respectively. One specific difference at the highest flow rate of 40 g/s, was that the inlet section of the channel (0~8 mm) is almost fully covered by the wetting front or liquid at all heat fluxes. This can be attributed to the wall heat flux not being high enough for significant vapor generation at this higher flow rate test case in comparison to the lower flow rate test cases.

The image data shows us that vapor patches and the wetting fronts move along the channel continuously providing all parts of the heated wall intermittent access to the incoming liquid. This access is provided at the wetting fronts and the wetting fronts are the locations of bubble nucleation and two-phase heat transfer will be dominant. Similar behavior was investigated by Thome et al. (2004) where they tried to estimate the heat transfer during evaporation in microchannels with intermittent boiling and vapor coverage on the heated surface. As depicted in Fig. 8, at any fixed location on the heated wall, the cooling process includes a vapor patch passing followed by a wetting front passing. This cycle repeats itself as continuous vapor patches and wetting fronts are generated and move along the channel. As the wall has access to vapor and wetting front over a cycle, the total time per cycle is

$$t_{total} = t_{dry} + t_{wet} \tag{5}$$

where t_{dry} and t_{wet} are defined as follows:

$$t_{dry} = \frac{\text{Length of dry surface}}{\text{Vapor velocity}} \tag{6}$$

and

$$t_{wet} = \frac{\text{Length of wetting front}}{\text{Liquid velocity}} \tag{7}$$

By calculating the time of wetting and the time of dry patch passing, we can calculate the time averaged heat transfer coefficients. The velocities here are not measured but computed based on the void fraction predictions from the vision tool as follows:

$$u_g = \frac{q''_w z}{\rho_g (\alpha H)(c_{p,f} \Delta T + h_{fg})}, \tag{8}$$

and

$$u_f = \frac{UH}{H - \alpha H} - \frac{q'' z}{\rho_f (H - \alpha H)(c_{p,f} \Delta T + h_{fg})}, \tag{9}$$

where u_g is the vapor velocity and u_f is the liquid velocity. The revised heat transfer coefficient can be expressed as the combination of single-phase and two-phase heat transfer coefficient based on the heated wall vapor and liquid access as follows:

$$h_{revised} = \frac{t_{dry}}{t_{total}} h_{sp} + \frac{t_{wet}}{t_{total}} h_{tp}. \tag{10}$$

In Eq. (10), h_{sp} is the single-phase heat transfer coefficient, and h_{tp} is the two-phase heat transfer coefficient. If the flow is laminar, the single-phase heat transfer coefficient is calculated using the following equation (Shah and London, 2014):

$$Nu = 8.235\left(1 - 1.883\beta + 3.767\beta^2 - 5.814\beta^3 + 5.361\beta^4 - 2.0\beta^5\right). \tag{11}$$

If the flow is turbulent, h_{sp} is calculated based on the famous Dittus-Boelter correlation (Dittus and Boelter, 1985). Two-phase heat transfer coefficient, h_{tp}, in Eq. (10) is calculated based on the original correlations listed in Table 2. Using Eq. (10), the revised heat transfer coefficients along the flow channel are plotted in Fig. 10(a) for the same test case shown in Fig. 7(a). Please note that the individual phase velocity data is only available when we have the film developing, hence the heat transfer model predictions begin after the initiation of the vapor film as depicted in Fig. 6. We can observe that the models now are able to clearly capture the reduction in trend in local hat transfer coefficient along the channel. It should be noted that the modification to heat transfer coefficient changed the average behaviors of heat transfer, but the trends are now more appropriate. There are clearly observable variations in predictions in the inlet section. For the inlet section, this can be attributed to our model equation assuming a two-phase heat transfer coefficient for the full inlet region even if the liquid might be subcooled and not boiling. However, as we are not demarcating an onset of nucleate boiling point, this result is expected. This error would not propagate downstream as boiling has initiated upstream for all other locations. For the downstream section. Similar comparison can be observed in Fig. 10(b) for the flow rate of 19.76 g/s even though the predictions are not as good as at the lower mass flow rate. Overall, for the complete dataset as shown in Table 2, the MAEs between the original

Table 2

Correlations for predicting heat transfer coefficient.

| Author(s)	Equation	Remarks	MAE$_{origin}$	MAE$_{revised}$
(Kim and Mudawar, 2013)	$h_{Kim} = \left(h_{nb}^2 + h_{cb}^2\right)^{0.5}$ $h_{cb} = \left[5.2\left(Bo\frac{P_H}{P_F}\right)^{0.08}We^{-0.54} + 3.5X_{tt}^{-0.94}\left(\frac{\rho_g}{\rho_f}\right)^{0.25}\right]\left(0.023Re_f^{0.8}Pr_f^{0.4}\frac{k_f}{D}\right)$ $h_{nb} = \left[2345\left(Bo\frac{P_H}{P_F}\right)^{0.7}P_R^{0.38}(1-x)^{-0.51}\right]\left(0.023Re_f^{0.8}Pr_f^{0.4}\frac{k_f}{D}\right)$ $Re_f = \frac{\rho_f u_f D_f}{\mu_f}$ $Bo = \frac{q''}{Gh_{fg}}$	D_h = 0.19-6.5 mm, FC72, R11, R113, R123, R1234yf, R1234ze, R134a, R152a, R22, R245fa, R32, R404A, R407C, R410A, R417A, CO_2, water	24.88 %	70.38 %
(Li and Wu, 2010)	$h_{Li} = 334Bo^{0.3}\left(BdRe_f^{0.36}\right)^{0.4}\frac{k_f}{D}, Bd = \frac{g(\rho_f - \rho_g)D^2}{\sigma}$	D_h = 0.16-3.1 mm, water refrigerants, FC-77, ethanol, propane, CO_2	23.38 %	57.50 %
(Oh and Son, 2010)	$h_{Oh} = 0.034Re_f^{0.8}Pr_f^{0.3}\left(1.58X_{tt}^{-0.87}\right)\left(\frac{k_f}{D}\right)$ $X_{tt} = \left(\frac{1-x}{x}\right)^{0.9}\left(\frac{\rho_f}{\rho_g}\right)^{0.5}\left(\frac{\mu_f}{\mu_g}\right)^{0.1}$	D= 1.77, 3.36, 5.35 mm, R134a, R22	89.92 %	97.67 %
(Tran et al., 1996)	$h_{Tran} = 8.4 \times 10^5\left(Bo^2We_f\right)^{0.3}\left(\rho_f/\rho_g\right)^{-0.4}, We_f = \frac{G^2D}{\rho_f\sigma}$	D= 2.46, 2.92 mm, D_h=2.40 mm, R12, R113	125.1 %	35.77 %
(Lazarek and Black, 1982)	$h_{Lazarek} = 30Bo^{0.714}Re_{fo}^{0.857}\frac{k_f}{D}, Re_{fo} = \frac{\rho_f u_f D}{\mu_f}$	D= 3.15 mm, R113	233.6 %	28.22 %
(Gopinath et al., 2002)	$h_{Warrier} = \left[1 + 6Bo^{1/16} - 5.3(1 - 855Bo)x^{0.65}\right]\left(0.023Re_f^{0.8}Pr_f^{0.4}\frac{k_f}{D}\right)$	D_h = 0.75 mm, FC84	36.55 %	55.85 %
(Liu and Winterton, 1991)	$h_{Liu} = \left[\left(Eh_{sp}\right)^2 + \left(Sh_{nb}\right)^2\right]^{0.5}$ $E = \left[1 + xPr_f\left(\frac{\rho_f}{\rho_g} - 1\right)\right]^{0.35}, h_{sp} = 0.023Re_f^{0.8}Pr_f^{0.4}\frac{k_f}{D}$ $S = \left(1 + 0.055E^{0.1}Re_f^{0.16}\right)^{-1}, h_{nb} = 55P_R^{0.12}\left(-\log_{10}P_R\right)^{-0.55}M^{-0.5}q''^{0.67}$	D= 2.95 – 32.0 mm, water, R11, R12, R13, R114, R22, ethylene, glycol	23.11 %	69.91 %
(Kenning and Cooper, 1989)	$h_{Kenning} = \left(1 + 1.8X_{tt}^{-0.87}\right)\left(0.023Re_f^{0.8}Pr_f^{0.4}\frac{k_f}{D}\right)$	D= 9.6-14.4 mm, water	67.20 %	89.91 %
(Agostini and Bontemps, 2005)	$h_{Agostini} = \begin{cases} 28q''^{2/3}G^{-0.26}x^{-0.1}, \text{for } x < 0.43 \\ 28q''^{2/3}G^{-0.64}x^{-2.08}, \text{for } x > 0.43 \end{cases}$	D_h = 2.01 mm, R134a	147.5 %	37.07 %
(Cooper, 1984)	$h_{Cooper} = 55P_R^{0.12}\left(-\log_{10}P_R\right)^{-0.55}M^{-0.5}q''^{0.67}$	6000 data points for nucleate boiling	21.96 %	68.23 %
(Yu et al., 2002)	$h_{Yu} = 30Re_{fo}^{0.857}Bo^{0.714}\left(\frac{1}{1-x}\right)^{0.143}\frac{k_f}{D}$	D= 3.15 mm, R113	234.5 %	28.24 %
(Hamdar et al., 2010)	$h_{Hamdar} = 6942.8\left(Bo^2We_f\right)^{0.2415}\left(\frac{\rho_g}{\rho_f}\right)^{0.22652}\frac{k_f}{D}$	D_h= 1.0 mm, R152a	15.88 %	64.51 %
(Sun and Mishima, 2009)	$h_{Sun} = 6\left(Re_{fo}^{1.05}Bo^{0.54}We_f^{-0.191}\right)\left(\frac{\rho_g}{\rho_f}\right)^{0.142}\frac{k_f}{D}$	D_h = 0.21-6.05 mm, R11, R12, R123, R134a, R141b, R22, R404a, R407c, R410a, CO_2, water	108.4 %	36.07 %
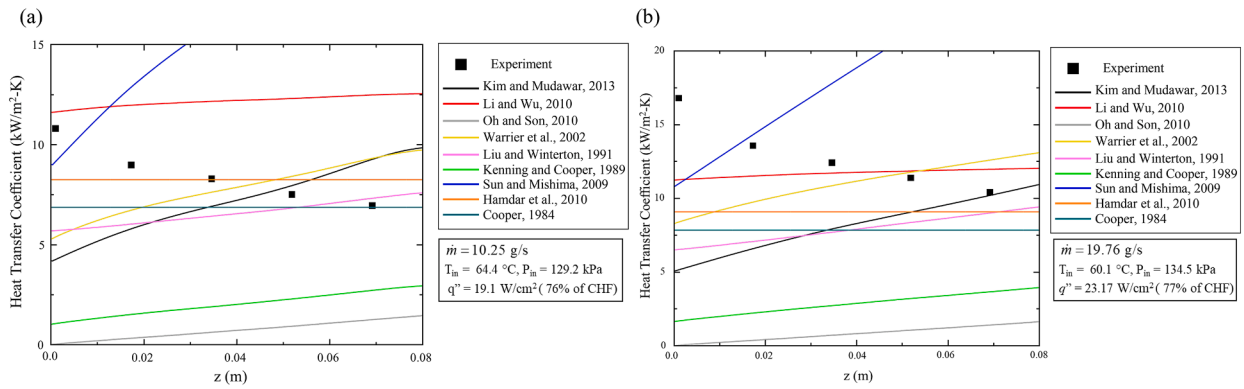
Fig. 7. Heat transfer coefficient comparison between experimental measurements and correlation predictions for (a) mass flow rate of 10.25 g/s with heat flux 76 % of CHF, and (b) mass flow rate of 19.76 with heat flux 77 % of CHF.
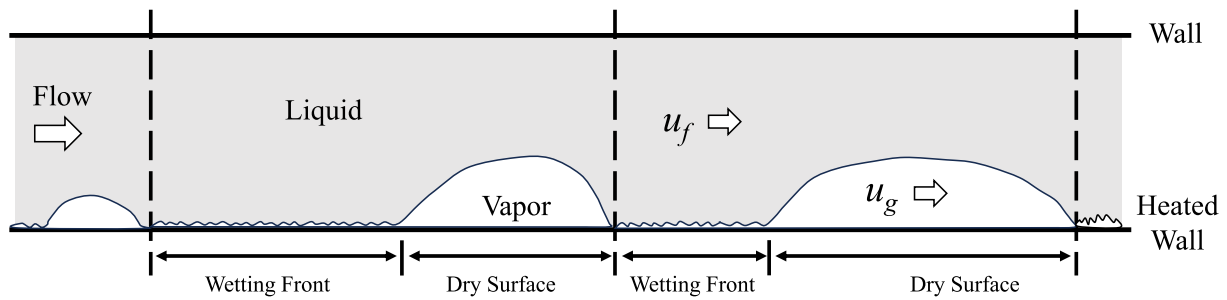

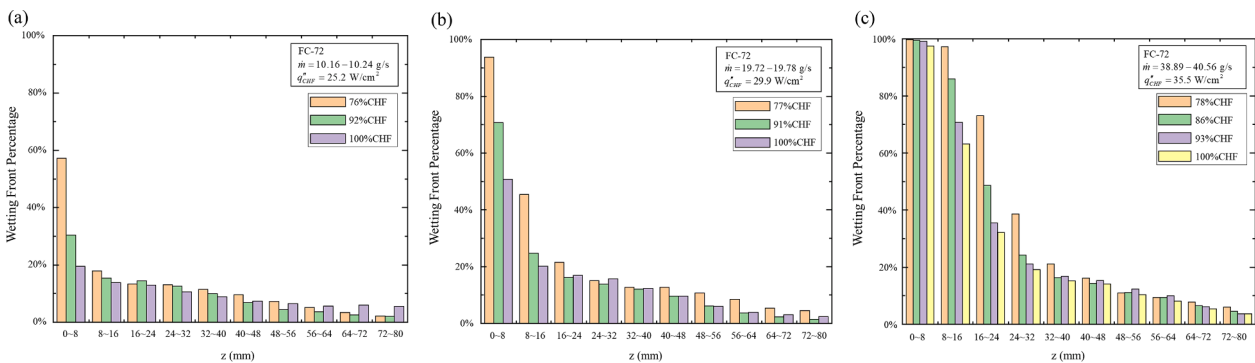**Fig. 8.** Schematic depicting the continuous wetting front and dry surface behavior observed along the flow channel.


Fig. 9. The ratios of wetting fronts in each 8 mm section of the flow channel for (a) mass flow rate around 10 g/s, (b) mass flow rate around 20 g/s, and (c) mass flow rate around 40 g/s

and the revised correlations show a change with some improving in predicting capability while others becoming worse. In addition, five representative correlations data for all test conditions are plotted in Fig. 10 (c). The best performing one shown is by Lazarek and Black (1982), while the worst performing is Oh and Son (2010). However, we can clearly see that the vision tool is helping us improve the capture of heat transfer trends.

Our approach to validating the heat transfer coefficient models is based on first comparing the experimental data to prior correlations which is a common approach in literature to validate them. The reason we use multiple correlations is to check which of the correlations best captures the experimental data obtained in our study. As can be seen in Table 2, none of the prior correlations have been developed specific to only our testing configuration and working fluid. The results from just testing these prior correlations show that not only do most of the correlations not capture the averaged data well, but they are also unable to capture the trend of reduction in heat transfer coefficient along the

channel observed in the experiments. With the use of extracted autonomous vision data on wetting fronts, we can enhance the correlations and show that we can better capture the heat transfer with most resulting correlations following the expected trends. However, as these correlations are not specific to our configuration, we still cannot select a correlation most applicable to our study based on this analysis.

In terms of limitations of this assessment, we need to understand that this effort in heat transfer coefficient assessment is preliminary because we directly used prior correlations developed for two-phase flow regimes in the wetting regions and supplemented with single-phase correlations in the dry regions to enhance predictions. With this assessment, we were able to understand the major shortcomings of prior correlations, but future efforts need to go into understanding the wetting front flow boiling behaviors in more detail to model the heat transfer accurately in that region. In addition, current wetting front data from flow visualization assumes that the side-view 2-dimensional flow imaging is sufficient to capture the 3-dimensions wetting behavior of the wall,
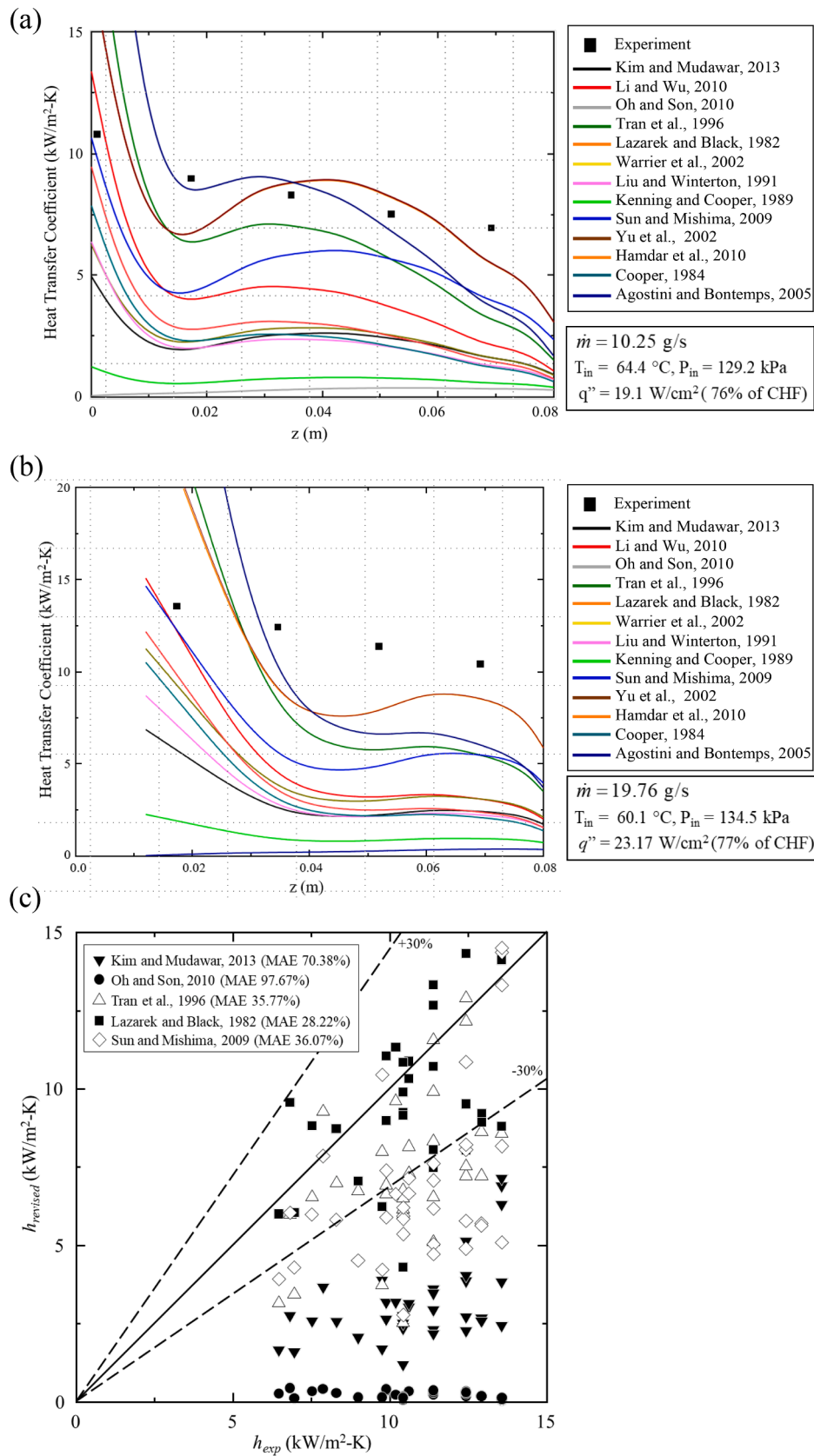
Fig. 10. Revised heat transfer coefficient comparisons between the experimental measurements and the correlation predictions for (a) mass flow rate of 10.25 g/s with heat flux 76 % of CHF, (b) mass flow rate of 19.76 g/s with heat flux 77 % of CHF (c) comparison between the experimental data and five correlation predictions.

which is not fully accurate. Therefore, this measurement needs refinement with better diagnostic measurements like wall phase distribution capture of the wetting region if we use a transparent heater.

4.3. Critical heat flux

CHF formulations are mostly based on mechanistic understanding of the trigger mechanism as discussed in Section 1.3 above and some correlations. We will limit ourselves to only validating with those models that can use data from our vision tool as input. In a very early study, Tong (1968) developed a correlation that predicts the CHF as follows,

$$q''_{CHF} = 0.23 f_o G h_{fg}\left[1 + 0.00216\left(\frac{p_{ex}}{P_{crit}}\right)^{1.8}\text{Re}^{0.5}Ja\right], \tag{12}$$

where

$$Ja = \frac{c_{p,f}(T_{sat} - T_{sub})}{h_{fg}}\frac{\rho_f}{\rho_g}, \tag{13}$$

and the Reynolds number is defined as

$$\text{Re} = \frac{GD}{\mu_f(1 - \alpha)}. \tag{14}$$

f_o is defined as

$$f_o = \frac{8(D_h/D_o)^{0.32}}{\text{Re}^{0.6}}, \tag{15}$$

where D_o is the reference diameter equal to 0.0127 m. Tong claims that the predicted CHF is based on the exit of the flow channel. Therefore, the captured void fraction at the outlet is applied to calculate the Reynolds number in Eq. (13) and the corresponding CHF. The predictions based on the revised and the original Tong model are shown in Table 3. The absolute errors for the revised Tong model ranges from 1.2 % to 38.2 %, while the absolute errors for the original Tong model ranges from 26.8 % to 54.3 %. The absolute error is defined by the following equation,

$$AbsoluteError = \frac{\left|CHF_{\text{exp}} - CHF_{pred}\right|}{CHF_{\text{exp}}}. \tag{16}$$

In another study, Liu and Nariai (2000) developed their model based on the observations of the vapor blanket and the liquid sublayer close to the heated wall. The final form of their CHF is given as follows,

$$q''_{CHF} = \frac{\rho_f \delta h_{fg}}{L_B}U_B, \tag{17}$$

where δ is the thickness of the sublayer, h_{fg} is the latent heat, L_B is the wavelength vapor blanket and U_B is the velocity of the vapor blanket. U_B is calculated by the following equation,

$$U_B = \frac{U_c}{1 + \rho_b}, \tag{18}$$

where

$$\rho_b = \sqrt{(\rho_c + \rho_g)/\rho_c}, \tag{19}$$

and U_c and ρ_c are the average velocity and average density of the core region, calculated by the following relation,

$$V_c = G/\rho_c, \tag{20}$$

and

$$\rho_c = (1 - \alpha)\rho_f + \alpha\rho_g. \tag{21}$$

Void fractions captured by our ML vision analysis are plugged into Eq. (21) to calculate the average density ρ_c. Average wavelengths data from our analysis are used to estimate the vapor blanket wavelengths. The predictions based on the revised and the original model by Liu et al. are also shown in Table 3. We see that there is a significant difference between model prediction and experimental measurements at the lowest mass flow rate. However, the predictions improve as the mass flow rate increases for the revised model.

Galloway and Mudawar (1993) postulated the *Interfacial Lift-off Model* by claiming that, just before CHF, bubbles would coalesce into long wavy vapor patches. The cooling happens in the wetting fronts between the patches. CHF occurs when the momentum of vapor produced in wetting fronts exceeds the pressure force induced across the vapor-liquid interface due to interfacial curvature. The CHF can be calculated as follows,

$$q''_{CHF} = \rho_g\left(c_{p,f}\Delta T_{sub,in} + h_{fg}\right)\left[\frac{4b\pi\sigma\sin(b\pi)}{\rho_g}\right]^{1/2}\left.\frac{\delta^{1/2}}{\lambda_{avg}}\right|_{z^*}, \tag{22}$$

where δ is the mean thickness of the vapor layer, λ_{avg} is the average wavelength, and b is the ratio of wetting front length to overall wavelength, which is assumed to be 0.2 in this original model. For the rigorous validation, input parameters to the *Interfacial Lift-off Model*, such as b, δ and λ_{avg} are computed using ML vision analysis as shown in Fig. 11. All three parameters are averaged for the entire flow channel. because the *Interfacial Lift-off Model* states that b and the δ/ λ_{avg} ratio are consistent along the channel length. Like other models, predictions seem to improve with increasing mass flow rate. For this model, the deviation at low mass flow rates can be attributed to the interfacial lift-off model being less applicable at lower flow rates as discussed by their authors (Zhang et al., 2005;). In addition, another reason for the lower accuracy is the assumption in the original model that the wetting front ratio is constant and equal to 0.2. We see from the data that this parameter is actually equal to 0.14, 0.2, and 0.46 for mass flow rates of 10, 20 and 40 g/s, respectively. It has to be noted that the original form of *Interfacial Lift-off Model* might not be able to capture the CHF trend as the mass flow rate increases due to the assumption of a constant wetting ratio 0.2.

In a recent study, Huang and Kharangate (2019), (2020) proposed the *Hydrodynamic Instability-based Model* to predict the CHF mechanism based on liquid access to the heated wall preventing CHF. They postulated that CHF occurs when liquid access is restricted in both the parallel to flow and perpendicular to the heated wall directions. Combining Taylor's stability wavelength criterion of the interface in the parallel direction with the Helmholtz instability of the interface in the perpendicular direction, the final form of the predicted CHF is expressed as

$$q''_{CHF} = \rho_g h_{fg}\frac{\pi}{16}\left(\frac{4\sigma}{\lambda_c}\right)^{1/2}\left[\left(\frac{\rho_f + \rho_g}{\rho_f\rho_g}\right)^{1/2} \middle/ \left(1 + \frac{\rho_g}{\rho_f}\frac{\pi}{16 - \pi}\right)\right]. \tag{23}$$

In this model the only unknown parameter is the critical wavelength, λ_c, which varies along the flow channel as seen in Fig. 12. Therefore, choosing the correct λ_c is important. According to Huang and Kharangate (2019), (2020), the *Hydrodynamic Instability-based Model*

Table 3
Experimental data and model predictions for CHF.

Mass flow rate (g/s)	10	20	40
Experimental measurement (W/cm²)	28.8	34.2	40.6
Original model by Tong (W/cm²)	36.5	46.3	62.6
Revised model by Tong (W/cm²)*	17.8	23.1	41.1
Original model by Liu et al. (W/cm²)	13.5	17.5	22.5
Revised model by Liu et al. (W/cm²)*	14.4	26.5	50.6
Original Interfacial Lift-off Model (W/cm²)	34.2	31.8	32.1
Revised Interfacial Lift-off Model (W/cm²)*	8.5	15.3	35.1
Original Hydrodynamic Instability-based Model (W/cm²)	22.4	25.0	29.6
Revised Hydrodynamic Instability-based Model (W/cm²)*	25.9	36.5	36.1

* Revised models use machine learning vision tool data we generate for predicting CHF in combination with their original formulations.
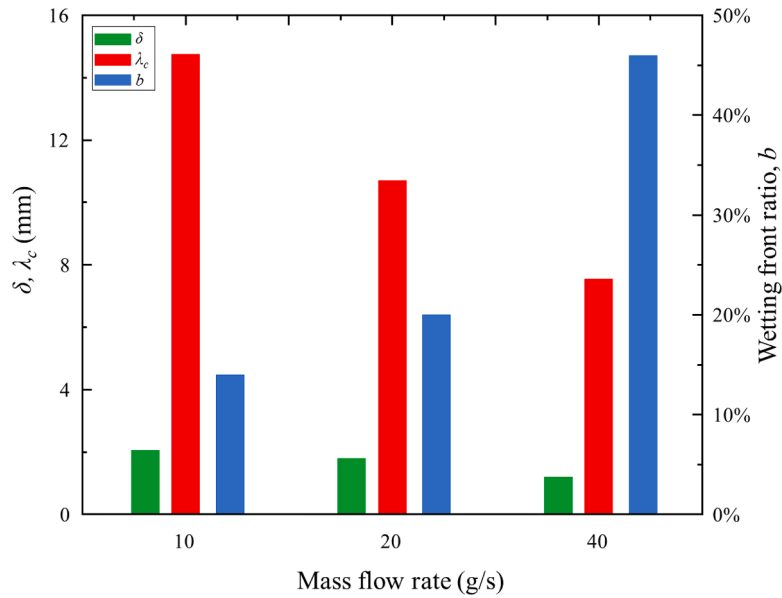
Fig. 11. Average wavelengths, wetting fronts, and wetting front ratios for the three flow rates at CHF based on the vision tool.
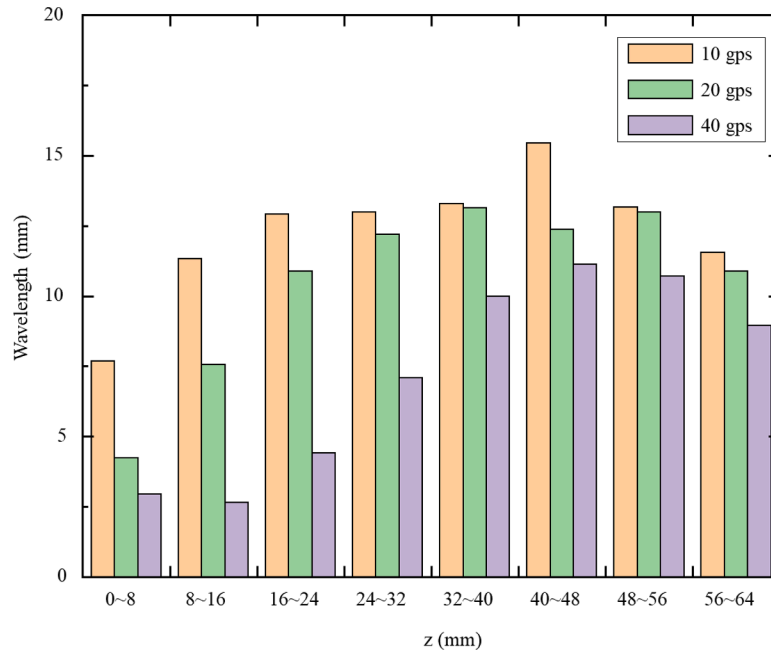

Fig. 12. Vapor wavelength variations along the flow channel over each 8 mm section at CHF for three mass flow rates.

provides the most conservative predictions of CHF by choosing the wavelengths in the upstream flow channel location. As the flow boiling process is pseudo-steady with the interface having a wavy behavior, to be consistent with the model, we need to capture the smallest wavelengths during this process. As the ML vision analysis provides a minimum wavelength for each frame in the 3,000 frames/second imaging data, we select the smallest 10 wavelengths in the inlet channel domain or the first 5 mm of the flow channel to compute the λ_c. The average is important because using the smallest wavelength might not be appropriate as a single frame data might be erroneous, while averaging 10 was selected as an appropriate number to capture the smallest wavelengths. It is observed that averaging the lowest 50 or 100 wavelengths, changes results slightly but the overall predictions from the model are similar. The corresponding CHF predictions are listed in Table 3. Good agreement is observed using this revised model with errors equal to 10 %, 7 %,

and 11 % for mass flow rates of 10, 20 and 40 g/s, respectively. This can be attributed to the model being less empirical and being specifically developed for a non-uniform heated rectangular configuration flow boiling configuration as investigated in this study. The original predictions based on the Hydrodynamic Instability-based Model are listed at the end of Table 3 for the comparison. The revised *Hydrodynamic Instability-based Model* performs better than its original model that estimates wavelength based on a combination of control volume and instability analysis.

Fig. 13 compares the predictions based on the four models where we use the vision data in combination with the mechanistic or semi-empirical formulations for predicting CHF from literature. Both the models by *Tong* and the model by *Liu et al.* are improved when using as input the experimental data from the vision tool. These models predict the CHF at the outlet based on the void fraction at the exit. By feeding
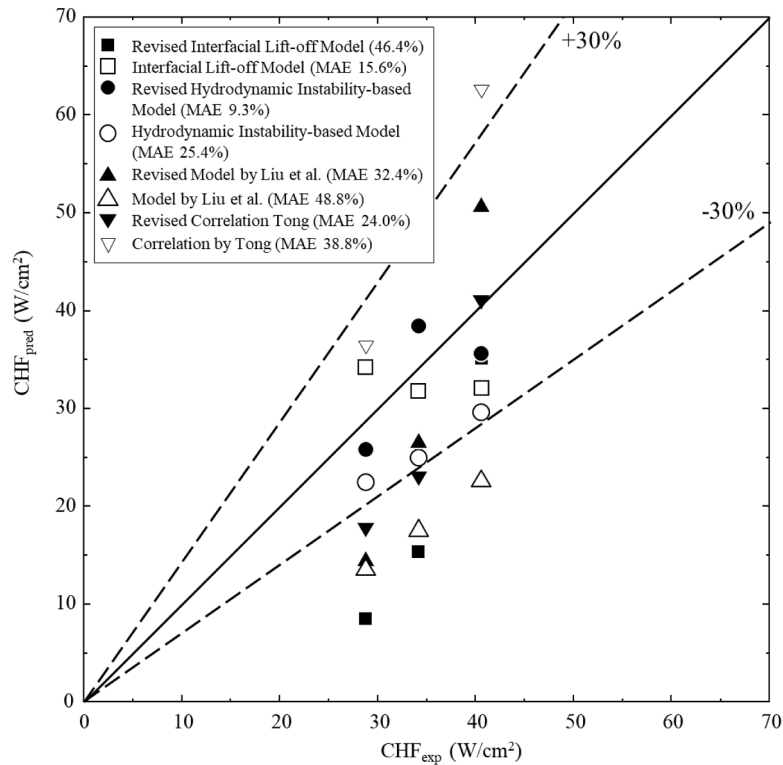
Fig. 13. Comparison between original and revised model predictions for CHF with experimental data.

the actual data, the accuracy of the models improves significantly. The *Interfacial Lift-off Model* predictions are slightly worse than that of the original model. However, the assumptions of wetting front ratio used in the original *Interfacial Lift-off Model* do not match the vision tool data on wetting front ratios observed. This shows the need for more validation in order to improve the model framework. the revised *Hydrodynamic Instability-based Model* with practical wavelengths improves the accuracy of the model.

In terms of the limitations of this assessment, we need to understand that the test cases under investigation here for CHF were limited to three flow rates drawing major conclusions. Even though the imaging data size and the time to train the models for that data were significant, the work was not validated for a wide range of testing and geometric conditions yet. In addition, similar to the heat transfer coefficient results, the 2-dimensional side view imaging data limits the capture of the statistical and accurate 3-dimensional wetting region waves data. This shortcoming can be improved in future studies by developing a transparent heater and capturing the wall phase distribution during flow boiling.

5. Needs for future studies based on limitations of the dataset

While this study shows that we can significantly improve the HTC or CHF models based on visual data, it should be noted that the models still need more data to be generalized for other conditions, including operating conditions and channel geometries.

This study focuses on the operating conditions in microgravity using data obtained from parabolic flights (Konishi et al., 2015). It emphasizes the impact of forces like fluid inertia, fluid viscosity, surface tension, and others rather than gravity for predicting performance parameters. Although the general modeling approach can be broadly applied, the modified models or correlations will not be generally applicable to all terrestrial conditions. For example, at high mass flow rates (≥ 20 g/s for our test channel), inertia dominates gravity and flow boiling behaviors in microgravity are similar to those in terrestrial conditions (Zhang

et al., 2007; Zhang et al., 2007; Konishi et al., 2013), making the ML framework applicable in these scenarios. More scenarios that combine various orientations, flow rates, and heating rates should be added to this work to improve the model generalizability.

Also, it should be noted that a limited dataset using a thin rectangular channel has been used in this study. With the current configuration, we assume that side-view 2-dimensional flow imaging is sufficient to capture the 3-dimensions wetting behavior of the wall for the collection of bubble-related statistical features. This assumption may not be necessarily accurate for different configurations, such as thicker channels, circular channels, or channels with 3D geometries. To gain full access to the visual information, it might be necessary to collect visual data from multiple views and angles, potentially with the implementation of transparent heaters.

It needs to be recognized that ML models may not work for completely unknown or unseen datasets. In the past, we have successfully shown our model works on two-phase flow configurations like pool boiling and dropwise condensation (Chang et al., 2023; Suh et al., 2021, 2024, 2021). To make this model work for our scenario, the previous ML frameworks based on pool boiling and dropwise condensation were re-trained by including thousands of images from the current microgravity flow boiling experiments at different mass flow rates and heat flux conditions, where a fine-tuning process is also performed to generate the final tool. Particularly, we train the ML model based on the convective boiling-dominant regime instead of the nucleate boiling-dominant regime. The execution of this additional step ensures that our model applies to similar scenarios. The nucleate boiling is presented by bubbly and slug flow while the convective boiling is shown as annular flows where the interfacial characteristics are extracted here. The nucleate or convective regimes are determined depending on the combination of working fluid, geometric, and operating conditions (Kim and Mudawar, 2013). Future studies need to add new data and perform new training to include more flow scenarios as well as other phase-change configurations.

Overall, this study shows how different theoretical models for

predicting flow boiling parameters can be improved with the use of ML vision data. This work can play a significant role in improving our mechanistic understanding and modeling capabilities for predicting individual performance parameters in flow boiling. However, there is a need to include more datasets in training across more testing conditions to make the ML vision framework more applicable and generalizable.

6. Conclusions

In this study we obtain physically meaningful features from ML enabled vision tools to validate models for estimating important performance parameters in flow boiling. Experimental features, such as void fraction, vapor and liquid wavelengths, wetting fronts, etc. are computed systematically using the autonomous vision tool and model formulations tested for the individual parameters, void fraction, heat transfer coefficients, and CHF. Key findings from the study are listed below.

1. ML-enabled vision framework computed two-phase features, such as void fraction along the channel for three flow rates and up to 4 heat flux scenarios. We validate 11 modeling formulations and correlations including the *Homogeneous Equilibrium Model* and the *Separated Flow Model,* where the *Separated Flow Model* shows the best performance evidenced by the lowest MAEs.
2. Conventional heat transfer coefficient correlations perform poorly in estimating the local heat transfer behavior along the channel and completely miss the trend in heat transfer coefficient variation along the channel. A novel approach which includes obtaining the ratio of the wetting front length and the dry surface length from the vision tool is proposed in this study. The resulting predictions of the revised heat transfer coefficient show significant improvement with the models being able to capture the trend observed in the experimental data.
3. Traditional CHF models were derived based on different trigger mechanisms. Assumptions and sub-models are needed to calculate the parameters. In the present study, we successfully reassess these CHF modeling frameworks by feeding features, such as void fraction, bubble wavelengths and wetting front ratios. The *Hydrodynamic Instability-based Model* shows the best performance among the 4 models that we have.
4. This work is laying the groundwork for further validation of larger flow boiling image datasets for better generalizability of the models.

CRediT authorship contribution statement

Cho-Ning Huang: Writing – original draft, Validation, Software, Methodology, Investigation, Formal analysis, Data curation. **Sanghyeon Chang:** Software, Formal analysis, Data curation. **Youngjoon Suh:** Writing – original draft, Software, Methodology, Formal analysis, Data curation. **Issam Mudawar:** Writing – original draft, Visualization, Resources. **Yoonjin Won:** Writing – original draft, Supervision, Software, Project administration, Funding acquisition. **Chirag R. Kharangate:** Writing – original draft, Supervision, Project administration, Methodology, Investigation, Funding acquisition, Conceptualization.

Declaration of competing interest

The authors declare the following financial interests/personal relationships which may be considered as potential competing interests:
Chirag Kharangate reports financial support was provided by Office of Naval Research. Yoonjin Won reports financial support was provided by Office of Naval Research. If there are other authors, they declare that they have no known competing financial interests or personal relationships that could have appeared to influence the work reported in this paper.

Data availability

The authors do not have permission to share data.

References

Agostini, B., Bontemps, A., 2005. Vertical flow boiling of refrigerant R134a in small channels. Int. J. Heat. Fluid Flow 26, 296–306.

Anand, R.S., Jawahar, C.P., Brusly Solomon, A., David, S., Bellos, E., Said, Z., 2022. Experimental investigations on modified thermosyphons using R134a/Al2O3 and comparative machine learning analysis. Appl. Therm. Eng. 212 https://doi.org/10.1016/j.applthermaleng.2022.118554.

Armand, A.A., Treščev, G.G., 1959. Investigation of the resistance during the movement of steam-water mixtures in a heated boiler pie at high pressure. Atomic Energy Res. Establ.

Bowring, R.W., 1972. A simple but accurate round tube, uniform heat flux, dryout correlation over the pressure range 0.7-17 MN/m 2 (100-2500 PSIA). UKAEA Reactor Group.

Cai, C., Mudawar, I., Liu, H., Xi, X., 2021. Assessment of void fraction models and correlations for subcooled boiling in vertical upflow in a circular tube. Int. J. Heat. Mass Transf. 171, 121060 https://doi.org/10.1016/J.IJHEATMASSTRANSFER.2021.121060.

Chang, S., Suh, Y., Shingote, C., Huang, C.-N., Mudawar, I., Kharangate, C., Won, Y., 2023. BubbleMask: Autonomous visualization of digital flow bubbles for predicting critical heat flux. Int. J. Heat. Mass Transf. 217, 124656 https://doi.org/10.1016/J.IJHEATMASSTRANSFER.2023.124656.

D. Chisholm, Two-phase flow in pipelines and heat exchangers, (No Title) (1983).

Collier, J.G., Thome, J.R., 1994. Convective Boiling and Condensation. Clarendon Press.

Cooper, M.G., 1984. Saturation nucleate pool boiling-a simple correlation. In: IChemE Symp. Ser., p. 786.

A.A.M. Delil, Variable Conductance Heat Pipes: Modelling and Applications, ICHMT Short Course on Passive Thermal Control, Antalya, Turkey (2003).

Dittus, F.W., Boelter, L.M.K., 1985. Heat transfer in automobile radiators of the tubular type. Int. Commun. Heat Mass Transf. 12, 3–22. https://doi.org/10.1016/0735-1933(85)90003-X.

Ducoulombier, M., Colasson, S., Bonjour, J., Haberschill, P., 2011. Carbon dioxide flow boiling in a single microchannel - Part II: Heat transfer. Exp. Therm. Fluid. Sci. 35, 597–611. https://doi.org/10.1016/j.expthermflusci.2010.11.014.

Escher, W., Michel, B., Poulikakos, D., 2009. Efficiency of optimized bifurcating tree-like and parallel microchannel networks in the cooling of electronics. Int. J. Heat. Mass Transf. 52, 1421–1430.

Fauske, H., 1961. Critical two-phase, steam–water flows. In: Proceedings of the 1961 Heat Transfer and Fluid Mechanics Institute. Stanford, CA. Stanford University Press, pp. 79–89.

Galloway, J.E., Mudawar, I., 1993. CHF mechanism in flow boiling from a short heated wall—II. Theoretical CHF model. Int. J. Heat. Mass Transf. 36, 2527–2540.

Ghahdarijani, A.M., Hormozi, F., Asl, A.H., 2017. Convective heat transfer and pressure drop study on nanofluids in double-walled reactor by developing an optimal multilayer perceptron artificial neural network. Int. Commun. Heat Mass Transf. 84, 11–19. https://doi.org/10.1016/J.ICHEATMASSTRANSFER.2017.03.014.

Gopinath, W.R., Dhir, V.K., Momoda, L.A., 2002. Heat transfer and pressure drop in narrow rectangular channels. Exp. Therm. Fluid Sci. 26 (1), 53–64.

Hamdar, M., Zoughaib, A., Clodic, D., 2010. Flow boiling heat transfer and pressure drop of pure HFC-152a in a horizontal mini-channel. Int. J. Refriger. 33, 566–577.

Horacek, B., Kiger, K.T., Kim, J., 2005. Single nozzle spray cooling heat transfer mechanisms. Int. J. Heat. Mass Transf. 48, 1425–1438.

Huang, C.N., Kharangate, C.R., 2019. A new mechanistic model for predicting flow boiling critical heat flux based on hydrodynamic instabilities. Int. J. Heat. Mass Transf. 138, 1295–1309. https://doi.org/10.1016/J.IJHEATMASSTRANSFER.2019.04.103.

Huang, C.N., Kharangate, C.R., 2020. Consolidated model for predicting flow boiling critical heat flux in single-sided and double-sided heated rectangular channels. Int. J. Heat. Mass Transf. 160, 120132 https://doi.org/10.1016/J.IJHEATMASSTRANSFER.2020.120132.

Huang, C.N., Lee, K.L., Tarau, C., Kamotani, Y., Kharangate, C., 2023. Thermal and hydrodynamic analysis of a self-purging hot reservoir variable conductance heat pipe. Appl. Therm. Eng. 226, 120346 https://doi.org/10.1016/J.APPLTHERMALENG.2023.120346.

Huang, C.N., Lee, K.L., Tarau, C., Kamotani, Y., Kharangate, C.R., 2021. Computational fluid dynamics model for a variable conductance thermosyphon. Case Stud. Therm. Eng. 25, 100960 https://doi.org/10.1016/J.CSITE.2021.100960.

Huang, L., El-Genk, M.S., 1994. Heat transfer of an impinging jet on a flat surface. Int. J. Heat. Mass Transf. 37, 1915–1923.

Huq, R., Loth, J.L., 1992. Analytical two-phase flow void prediction method. J. Thermophys. Heat. Trans. 6, 139–144.

Katto, Y., 1981. General features of CHF of forced convection boiling in uniformly heated rectangular channels. Int. J. Heat. Mass Transf. 24, 1413–1419.

Katto, Y., Ohno, H., 1984. An improved version of the generalized correlation of critical heat flux for the forced convective boiling in uniformly heated vertical tubes. Int. J. Heat. Mass Transf. 27, 1641–1648.

Kawahara, A., Chung, P.Y., Kawaji, M., 2002. Investigation of two-phase flow pattern, void fraction and pressure drop in a microchannel. Int. J. Multiph. Flow 28, 1411–1435. https://doi.org/10.1016/S0301-9322(02)00037-X.

Kenning, D.B.R., Cooper, M.G., 1989. Saturated flow boiling of water in vertical tubes. Int. J. Heat. Mass Transf. 32, 445–458. https://doi.org/10.1016/0017-9310(89)90132-4.

Kew, P.A., Cornwell, K., 1997. Correlations for the prediction of boiling heat transfer in small-diameter channels. Appl. Therm. Eng. 17, 705–715.

Kharangate, C.R., Konishi, C., Mudawar, I., 2016. Consolidated methodology to predicting flow boiling critical heat flux for inclined channels in Earth gravity and for microgravity. Int. J. Heat. Mass Transf. 92, 467–482. https://doi.org/10.1016/j.ijheatmasstransfer.2015.08.018.

Kharangate, C.R., O'Neill, L.E., Mudawar, I., Hasan, M.M., Nahra, H.K., Balasubramaniam, R., Hall, N.R., Macner, A.M., Mackey, J.R., 2015. Flow boiling and critical heat flux in horizontal channel with one-sided and double-sided heating. Int. J. Heat. Mass Transf. 90, 323–338. https://doi.org/10.1016/J.IJHEATMASSTRANSFER.2015.06.073.

Khosravi, A., Pabon, J.J.G., Koury, R.N.N., Machado, L., 2018. Using machine learning algorithms to predict the pressure drop during evaporation of R407C. Appl. Therm. Eng. 133, 361–370. https://doi.org/10.1016/J.APPLTHERMALENG.2018.01.084.

Kim, J., 2007. Spray cooling heat transfer: The state of the art. Int. J. Heat. Fluid. Flow. 28, 753–767.

Kim, S.M., Mudawar, I., 2013. Universal approach to predicting saturated flow boiling heat transfer in mini/micro-channels – Part II. Two-phase heat transfer coefficient. Int. J. Heat. Mass Transf. 64, 1239–1256. https://doi.org/10.1016/j.ijheatmasstransfer.2013.04.014.

Konishi, C., Lee, H., Mudawar, I., Hasan, M.M., Nahra, H.K., Hall, N.R., Wagner, J.D., May, R.L., Mackey, J.R., 2015. Flow boiling in microgravity: Part 1–Interfacial behavior and experimental heat transfer results. Int. J. Heat. Mass Transf. 81, 705–720.

Konishi, C., Lee, H., Mudawar, I., Hasan, M.M., Nahra, H.K., Hall, N.R., Wagner, J.D., May, R.L., Mackey, J.R., 2015. Flow boiling in microgravity: Part 2 - Critical heat flux interfacial behavior, experimental data, and model. Int. J. Heat. Mass Transf. 81, 721–736. https://doi.org/10.1016/j.ijheatmasstransfer.2014.10.052.

Konishi, C., Mudawar, I., Hasan, M.M., 2013. Criteria for negating the influence of gravity on flow boiling critical heat flux with two-phase inlet conditions. Int. J. Heat. Mass Transf. 65, 203–218.

Koşar, A., Kuo, C.-J., Peles, Y., 2005. Boiling heat transfer in rectangular microchannels with reentrant cavities. Int. J. Heat. Mass Transf. 48, 4867–4886.

Kutateladze, S.S., Leont'ev, A.I., 1966. Some applications of the asymptotic theory of the turbulent boundary layer. In: International Heat Transfer Conference Digital Library. Begel House Inc.

G.M. Lazarek, S.H. Black, Evaporative heat transfer, pressure drop and critical heat flux in a small vertical tube with R-l 13, 1982.

Lee, C.H., Mudawwar, I., 1988. A mechanistic critical heat flux model for subcooled flow boiling based on local bulk flow conditions. Int. J. Multiph. Flow 14, 711–728. https://doi.org/10.1016/0301-9322(88)90070-5.

Li, J., O'Neill, L.E., Izenson, M.G., Kharangate, C.R., 2023. Data consolidation, correlations assessment, and new correlation development for pool boiling critical heat flux specific to cryogenic fluids. Int. J. Heat. Mass Transf. 213, 124315 https://doi.org/10.1016/J.IJHEATMASSTRANSFER.2023.124315.

Li, W., Wu, Z., 2010. A general criterion for evaporative heat transfer in micro/mini-channels. Int. J. Heat. Mass Transf. 53, 1967–1976. https://doi.org/10.1016/j.ijheatmasstransfer.2009.12.059.

Liu, W., Nariai, H., Inasaka, F., 2000. Prediction of critical heat flux for subcooled flow boiling. Int. J. Heat Mass Transf. 43 (18), 3371–3390.

Liu, Z., Winterton, R.H.S., 1991. A general correlation for saturated and subcooled flow boiling in tubes and annuli, based on a nucleate pool boiling equation. Int. J. Heat. Mass Transf. 34, 2759–2766. https://doi.org/10.1016/0017-9310(91)90234-6.

Mehrabi, M., Sharifpur, M., Meyer, J.P., 2013. Modelling and multi-objective optimisation of the convective heat transfer characteristics and pressure drop of low concentration TiO2–water nanofluids in the turbulent flow regime. Int. J. Heat. Mass Transf. 67, 646–653. https://doi.org/10.1016/J.IJHEATMASSTRANSFER.2013.08.013.

Nair, A., Ramkumar, P., Mahadevan, S., Prakash, C., Dixit, S., Murali, G., Vatin, N.I., Epifantsev, K., Kumar, K., 2022. Machine learning for prediction of heat pipe effectiveness. Energies (Basel) 15. https://doi.org/10.3390/en15093276.

Naphon, P., Wiriyasart, S., Arisariyawong, T., 2018. Artificial neural network analysis the pulsating Nusselt number and friction factor of TiO2/water nanofluids in the spirally coiled tube with magnetic field. Int. J. Heat. Mass Transf. 118, 1152–1159. https://doi.org/10.1016/J.IJHEATMASSTRANSFER.2017.11.091.

Oh, C.H., Englert, S.B., 1993. Critical heat flux for low flow boiling in vertical uniformly heated thin rectangular channels. Int. J. Heat. Mass Transf. 36, 325–335.

Oh, H.K., Son, C.H., 2010. New correlation to predict the heat transfer coefficient in-tube cooling of supercritical CO2 in horizontal macro-tubes. Exp. Therm. Fluid. Sci. 34, 1230–1241. https://doi.org/10.1016/J.EXPTHERMFLUSCI.2010.05.002.

Ohadi, M., Choo, K., Dessiatoun, S., Cetegen, E., 2013. Next Generation Microchannel Heat Exchangers. Springer.

Okawa, T., 2012. Onset of nucleate boiling in mini and microchannels: A brief review. Front. Heat Mass Transf. 3 https://doi.org/10.5098/hmt.v3.1.3001.

Polat, S., Huang, B., Mujumdar, A.S., Douglas, W.J.M., 1989. Numerical flow and heat transfer under impinging jets: a review. Ann. Rev. Heat Transf. 2.

Qiu, Y., Garg, D., Kim, S.M., Mudawar, I., Kharangate, C.R., 2021. Machine learning algorithms to predict flow boiling pressure drop in mini/micro-channels based on universal consolidated data. Int. J. Heat. Mass Transf. 178, 121607 https://doi.org/10.1016/J.IJHEATMASSTRANSFER.2021.121607.

Ren, S., He, K., Girshick, R., Sun, J., 2015. Faster r-cnn: Towards real-time object detection with region proposal networks. Adv. Neural. Inf. Process. Syst. 28.

Rohuani, Z., Axelsson, E., 1970. Calculation of volume void fraction in a subcooled and quality region. Int. J. Heat. Mass Transf. 17, 383–393.

Sauciuc, I., Akbarzadeh, A., Johnson, P., 1996. Temperature control using variable conductance closed two-phase heat pipe. Int. Commun. Heat Mass Transf. 23, 427–433. https://doi.org/10.1016/0735-1933(96)00028-0.

Schrage, D.S., Hsu, J., Jensen, M.K., 1988. Two-phase pressure drop in vertical crossflow across a horizontal tube bundle. AIChE J. 34, 107–115.

Shah, M.M., 1982. Chart correlation for saturated boiling heat transfer: equations and further study. ASHRAE Trans. (United States) 88.

Shah, R.K., London, A.L., 2014. Laminar Flow Forced Convection in Ducts: a Source Book for Compact Heat Exchanger Analytical Data. Academic Press.

Smith, S.L., 1969. Void fractions in two-phase flow: a correlation based upon an equal velocity head model. Proc. Instit. Mech. Eng. 184, 647–664.

Suh, Y., Bostanabad, R., Won, Y., 2021. Deep learning predicts boiling heat transfer. Sci. Rep. 11, 5622.

Suh, Y., Chang, S., Simadiris, P., Inouye, T.B., Hoque, M.J., Khodakarami, S., Kharangate, C., Miljkovic, N., Won, Y., 2024. VISION-iT: A framework for digitizing bubbles and droplets. Energy AI 15, 100309.

Y. Suh, S. Chang, P. Simadiris, T. Inouyet, M.J. Hoque, S. Khodakarami, C. Kharangate, N. Miljkovic, Y. Won, VISION-iT: Deep nuclei tracking framework for digitalizing bubbles and droplets, Available at SSRN 4491956 (2023).

Suh, Y., Lee, J., Simadiris, P., Yan, X., Sett, S., Li, L., Rabbi, K.F., Miljkovic, N., Won, Y., 2021. A deep learning perspective on dropwise condensation. Adv. Sci. 8, 2101794.

Sun, L., Mishima, K., 2009. An evaluation of prediction methods for saturated flow boiling heat transfer in mini-channels. Int. J. Heat Mass Transf. 52, 5323–5329. 10.1016/j.ijheatmasstransfer.2009.06.041.

Tan, L., Chen, C., Dong, X., Gong, Z., Wang, M., 2017. Experimental study on CHF of R134a flow boiling in a horizontal helically-coiled tube near the critical pressure. Exp. Therm. Fluid. Sci. 82, 472–481.

Thome, J.R., Dupont, V., Jacobi, A.M., 2004. Heat transfer model for evaporation in microchannels. Part I: Presentation of the model. Int. J. Heat. Mass Transf. 47, 3375–3385. https://doi.org/10.1016/j.ijheatmasstransfer.2004.01.006.

Tong, L.S., 1968. Boundary-layer analysis of the flow boiling crisis. Int. J. Heat. Mass Transf. 11, 1208–1211.

T.N. Tran, M.W. Wambsganss, D.M. France, Small circular-and rectangular-channel boiling with two refrigerants, 1996.

Weisman, J., Pei, B.S., 1983. Prediction of critical heat flux in flow boiling at low qualities. Int. J. Heat. Mass Transf. 26, 1463–1477. https://doi.org/10.1016/S0017-9310(83)80047-7.

Yu, W., France, D.M., Wambsganss, M.W., Hull, J.R., 2002. Two-phase pressure drop, boiling heat transfer, and critical heat flux to water in a small-diameter horizontal tube. INT. J. MULTIPHAS. FLOW 28 (6), 927–941.

Zhang, H., Mudawar, I., Hasan, M.M., 2002. Experimental and theoretical study of orientation effects on flow boiling CHF. Int. J. Heat. Mass Transf. 45, 4463–4477.

Zhang, H., Mudawar, I., Hasan, M.M., 2005. Flow boiling CHF in microgravity. Int. J. Heat. Mass Transf. 48, 3107–3118.

Zhang, H., Mudawar, I., Hasan, M.M., 2007. Assessment of dimensionless CHF correlations for subcooled flow boiling in microgravity and Earth gravity. Int. J. Heat. Mass Transf. 50, 4568–4580.

Zhang, H., Mudawar, I., Hasan, M.M., 2007. CHF model for subcooled flow boiling in Earth gravity and microgravity. Int. J. Heat. Mass Transf. 50, 4039–4051.

S.M. Zivi, Estimation of steady-state steam void-fraction by means of the principle of minimum entropy production, (1964).

Zuber, N., Findlay, J.A., 1965. Average volumetric concentration in two-phase flow systems. J. Heat. Transf. 87, 453–468. https://doi.org/10.1115/1.3689137.

西野晴生, 山崎彌三郎, 1963. 沸騰系における蒸気体積率の新推算法. 日本原子力学会誌 5, 39–46. https://doi.org/10.3327/jaesj.5.39.